iScience

CellPress
OPEN ACCESS

Article

Controlled Transdermal Release of Antioxidant Ferulate by a Porous Sc(III) MOF

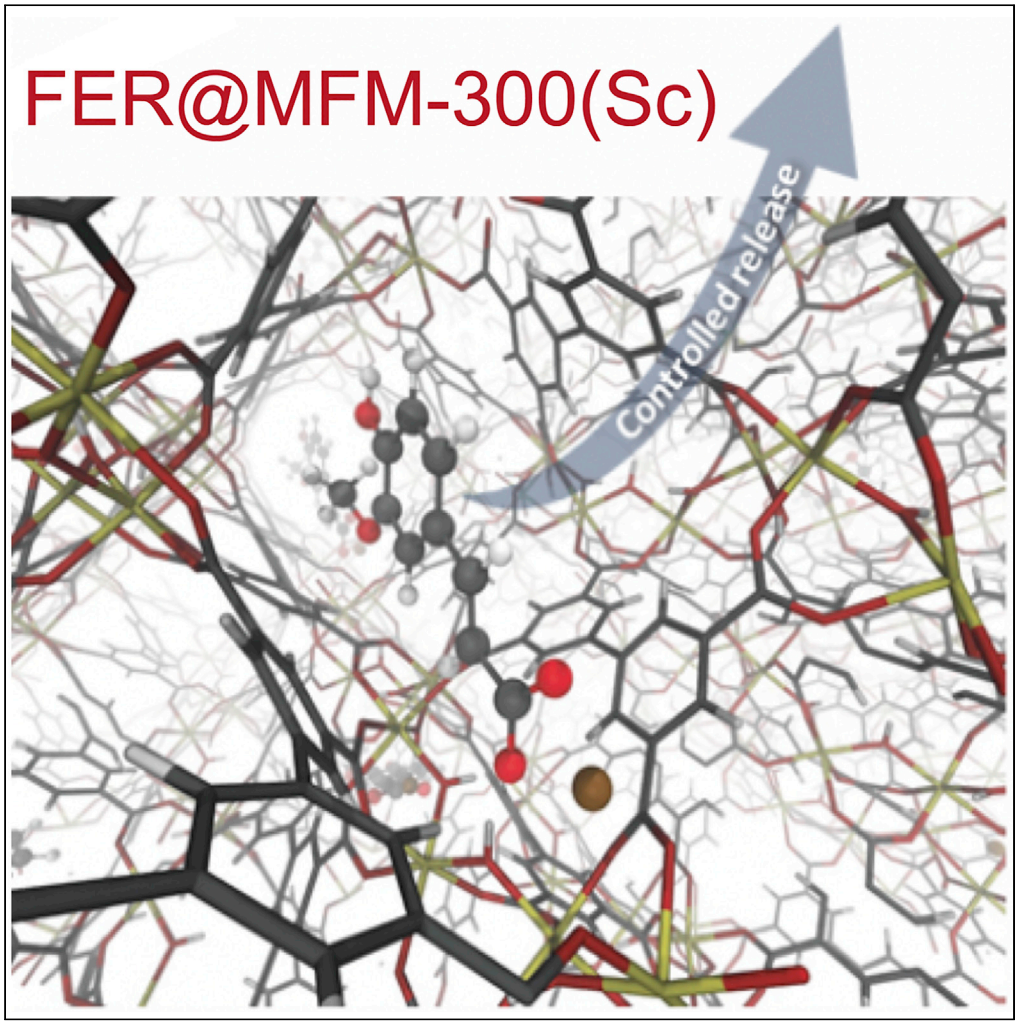

Génesis Osorio-Toribio, Miriam de J. Velásquez-Hernández, Paulo G.M. Mileo, ..., Guillaume Maurin, Enrique Lima, Ilich A. Ibarra

guillaume.maurin1@umontpellier.fr (G.M.)
lima@iim.unam.mx (E.L.)
argel@unam.mx (I.A.I.)

HIGHLIGHTS

MFM-300(Sc) presents good stability and biocompatibility

FER@MFM-300(Sc) allows the long-term transdermal release of ferulate (FER^-)

FER@MFM-300(Sc) prevents the photodegradation of FER

Osorio-Toribio et al., iScience *23*, 101156
June 26, 2020 Crown

https://doi.org/10.1016/j.isci.2020.101156

iScience

CellPress
OPEN ACCESS

Article

Controlled Transdermal Release of Antioxidant Ferulate by a Porous Sc(III) MOF

Génesis Osorio-Toribio,[1,11] Miriam de J. Velásquez-Hernández,[2,11] Paulo G.M. Mileo,[3] J. Antonio Zárate,[1,3] Javier Aguila-Rosas,[1,4] Gerardo Leyva-Gómez,[5] Roberto Sánchez-Sánchez,[6] Jonathan J. Magaña,[7] Mario Alberto Pérez-Díaz,[8] Isabel Abánades Lázaro,[9,10] Ross S. Forgan,[10] Guillaume Maurin,[3,*] Enrique Lima,[1,*] and Ilich A. Ibarra[1,12,*]

SUMMARY

The Sc(III) MOF-type MFM-300(Sc) is demonstrated in this study to be stable under physiological conditions (PBS), biocompatible (to human skin cells), and an efficient drug carrier for the long-term controlled release (through human skin) of antioxidant ferulate. MFM-300(Sc) also preserves the antioxidant pharmacological effects of ferulate while enhancing the bio-preservation of dermal skin fibroblasts, during the delivery process. These discoveries pave the way toward the extended use of Sc(III)-based MOFs as drug delivery systems (DDSs).

INTRODUCTION

Metal-organic frameworks (MOFs) are one of the most recent classes of porous materials integrating a unique chemical and topological richness with an almost infinite combination of metal ions and multidentate organic linkers (Furukawa et al., 2013; Jiang et al., 2016; Kitagawa et al., 2004). This family of porous solids first seen as a curiosity in the field of materials science, has been envisaged for further applications, including but not limited to, gas storage (Makal et al., 2012; Murray et al., 2009; Suh et al., 2012), catalysis (Li et al., 2012; Sumida et al., 2012; Wu et al., 2012), sensors (Chen et al., 2010a; Cui et al., 2012; Kreno et al., 2012; Tchalala et al., 2019), electrical conductivity (Sheberla et al., 2014, 2017), and drug delivery (Chen and Wu, 2018; Horcajada et al., 2012; Simon-Yarza et al., 2018). Some of these hybrid materials combine outstanding adsorption/separation performances of highly challenging molecules with green synthesis and easy scale-up that make them highly attractive to address a large panel of social concerns (Chen and Wu, 2018; Horcajada et al., 2012; Simon-Yarza et al., 2018). In particular, MOFs show great potential for the design of modern drug delivery technologies (Chen and Wu, 2018; Horcajada et al., 2012; Jie and Ying-Wei, 2020; Simon-Yarza et al., 2018; Tibbetts and Kostakis, 2020). Unlike conventional drug carriers envisaged so far, e.g., micelles, liposomes, dendrimers, and mesoporous silica nanoparticles (Gillies and Fréchet, 2005; Porter et al., 2007; Senapati et al., 2018; Zhang and Ma, 2013; Zhang et al., 2012), MOFs offer a unique opportunity to modulate the incorporated drug payload and release kinetics by a fine engineering of their pore dimension (size/shape) and a fine-tuning of the nature/strength of the adsorption sites decorating their internal pore walls as well as of the functionalization of their external surfaces (Liang et al., 2019). The high degree of variability targets an efficient encapsulation of a broad range of highly challenging active pharmaceutical ingredients (APIs) in order to enhance their bioavailability and "shelf life" (Chen et al., 2018; Giménez-Marqués et al., 2016; Horcajada et al., 2010; Liu et al., 2019; Luo et al., 2019; Teplensky et al., 2017; Wang et al., 2018; Xiao-Gang et al., 2019; Ya-Pan et al., 2019; Ying et al., 2019). Cargo drug loading in MOFs can be accomplished either by an encapsulation during the synthesis (Doonan et al., 2017; Liang et al., 2015, 2019), or by a post-synthetic infiltration in the porosity of already-formed architectures (Chen et al., 2018; Horcajada et al., 2010; Teplensky et al., 2017; Wang et al., 2018). This later strategy has been widely explored in the development of controlled drug delivery systems (DDSs) of diverse natures for a large number of therapeutic agents. However, when contemplating any nano-carrier materials for biomedical applications several criteria are desired: (1) achieving an optimal drug loading efficiency (Horcajada et al., 2012), (2) allowing the protection of the drug to avoid any degradation under physiological media, (3) ensuring a gradual release of the drug once administrated to circumvent a "burst release effect" (Bellido et al., 2014; Li et al., 2017; Ruyra et al., 2015; Velásquez-Hernández et al., 2019), and (4) not having toxic effects on the body. In this context, a number of porous MOFs, built up from bio-compatible metal

[1]Laboratorio de Fisicoquímica y Reactividad de Superficies (LaFReS), Instituto de Investigaciones en Materiales, Universidad Nacional Autónoma de México, Ciudad de México, Mexico

[2]Institute of Physical and Theoretical Chemistry, Graz University of Technology, Stremayrgasse 9, 8010 Graz, Austria

[3]ICGM, Univ. Montpellier, CNRS, ENSCM, Montpellier, France

[4]Departamento de Sistemas Biológicos, Universidad Autónoma Metropolitana-Azcapotzalco, Ciudad de México, Mexico

[5]Departamento de Farmacia, Facultad de Química, Universidad Nacional Autónoma de México, Ciudad de México, México

[6]Unidad de Ingeniería de Tejidos Terapia Celular y Medicina Regenerativa Instituto Nacional de Rehabilitación Luis Guillermo Ibarra Ibarra (INR-LGII), Ciudad de México, Mexico

[7]Laboratorio de Medicina Genómica, Instituto Nacional de Rehabilitación Luis Guillermo Ibarra Ibarra (INR-LGII), Ciudad de México, Mexico

[8]Laboratorio de Biomembranas, Escuela Nacional de Ciencias Biológicas, Instituto Politécnico Nacional, Ciudad de México, Mexico

[9]Universidad de Valencia (ICMol), Catedrático José Beltrán-2, Paterna, Spain

[10]WestCHEM School of Chemistry, University of Glasgow, Joseph Black

Continued

ions, i.e., Ca(II), Mg(II), Zn(II), Zr(IV), Ti(III), and Fe(III), has been discovered (Chen and Wu, 2018; Chen et al., 2018; Doonan et al., 2017; Horcajada et al., 2010, 2012; Liang et al., 2015, 2019; Simon-Yarza et al., 2018; Teplensky et al., 2017; Wang et al., 2018). However, only a small fraction of them encompass the adequate features to fulfill all requirements mentioned above (Chen and Wu, 2018; Horcajada et al., 2012; Simon-Yarza et al., 2018). Typically, most of these MOFs suffer from a fast degradation in presence of phosphates, essential components in body fluids, hampering their applications for controlled drug delivery (Bellido et al., 2014; Li et al., 2017; Ruyra et al., 2015; Velásquez-Hernández et al., 2019). The collapse of the framework is induced by a highly favorable complexation of the phosphate species to most of the metal centers tested so far, e.g., Zr(IV), Fe(III), and Zn(II) (Bellido et al., 2014; Li et al., 2017; Ruyra et al., 2015; Velásquez-Hernández et al., 2019).

In this context, Sc(III)-MOFs have never been investigated for drug delivery applications to date. This is likely mostly a result of the controversy on the bio-compatible nature of this metal. On the one hand, Sc(III) was demonstrated to be reactive toward proteins owing to its ability to replace Ca(II) in many biochemical events causing negative effects in enzyme systems and cell metabolism (Ford-Hutchinson and Perkins, 1971; Sánchez-González et al., 2013). On the other hand, Sc(III) is successfully used as a radioactive isotope in medical applications (Horovitz, 2012; Szkliniarz et al., 2016), and a low concentration of Sc(III) was proven to positively enhance specific antibiotic overproduction and have beneficial antibacterial effect (Kawai et al., 2007). Therefore, this critically urges for a comprehensive study on Sc(III) MOFs for potential drug delivery applications to address these open questions.

The present work reports the applicability of MFM-300(Sc), also denoted NOTT-400 (Ibarra et al., 2011), as drug carrier for transdermal administration of ferulic acid (FA). FA is a natural superior antioxidant since its phenolic nucleus and unsaturated side chain allow the formation of resonance-stabilized phenoxy radical acting as free radical scavenger (Antolovich et al., 2004; Chen et al., 2010b; Zduńska et al., 2018). FA also exhibits anti-diabetic, anti-cardiovascular, and anti-inflammatory properties (Antolovich et al., 2004; Chen et al., 2010b; Zduńska et al., 2018). Interestingly, this molecule has a protective role for the main skin structures such as collagen, fibroblasts, keratinocytes, and elastin (Zih-yi et al., 2019). Consequently, this therapeutic agent has been widely used in skin care formulations as photoprotective agent and delayer of skin photoaging processes and in the treatment of rosacea (Antolovich et al., 2004; Chen et al., 2010b; Zduńska et al., 2018). Owing to the importance of FA as active ingredient in a variety of cosmetic products, transdermal delivery is the most common administration route (Zih-yi et al., 2019). However, on premature exposure to sunlight FA undergoes oxidation reactions leading to the formation of quinones, dimers, and aldehydes (Antolovich et al., 2004). The photodegradation of FA not only limits its shelf-life but also reduces its effectiveness before it permeates the *stratum corneum* (SC) (Antolovich et al., 2004), which is the most superficial layer of the epidermis, and acts as skin barrier (Kalpana et al., 2010; Pegoraro et al., 2012). In order to circumvent these limitations, herein, we propose to encapsulate FA in the pores of MFM-300(Sc) with the main idea to prevent the photodegradation process of FA and to allow its continuous and sustained release over time that does not require frequent dosing.

RESULTS AND DISCUSSION

MFM-300(Sc) as Drug Carrier of FA (FER^-)

MFM-300(Sc) of chemical formula $[Sc_2(BPTC)(OH)_2]$, was synthesized and activated according to a previously reported procedure (Supplemental Information) (Ibarra et al., 2011). A series of characterization tools confirmed the phase purity of the material and the full activation of its porosity (see Supplemental Information). This MOF crystallizes in the chiral tetragonal space group $I4_122$, with each $[Sc_2(\mu\text{-OH})]$ (Figure S1) binuclear center octahedrally coordinated to six O-donors, four from four different carboxylate groups of $BPTC^{-4}$ ligand ($BPTC^{-4}$, biphenyl-3,3′,5,5-tetracarboxylate) and two from two different μ-OH groups, leading to a 3D framework with a channel of about 8.1 Å (Figure S1) (Ibarra et al., 2011). To evaluate the capacity of MFM-300(Sc) as drug delivery carrier, ferulic acid was initially loaded as ferulate species (FER^-) (*vide infra*) within the MOF by a simple impregnation process, i.e., aqueous solution of ferulic acid (FA) at pH = 9 (Supplemental Information). Since the pore opening of MFM-300(Sc) exceeds the dimension of the drug (10.0 × 7.1 × 1.8 $Å^3$), FER^- is expected to be confined in its channels. UV-vis absorption spectroscopy was employed to monitor the concentration of FER^- during the impregnation process (Figure S2). The maximum FER^- payload (16.1 wt%) was achieved after 5 days of incubation; we determined this percentage by quantifying free FER^- in the supernatants when the MOF dispersion was centrifuged (Supplemental Information). The drug content was further corroborated by TGA analysis (Figure S5). Powder X-ray

Building, University Avenue, Glasgow G12 8QQ, UK

[11]These authors contributed equally

[12]Lead Contact

*Correspondence: guillaume.maurin1@umontpellier.fr (G.M.), lima@iim.unam.mx (E.L.), argel@unam.mx (I.A.I.)

https://doi.org/10.1016/j.isci.2020.101156

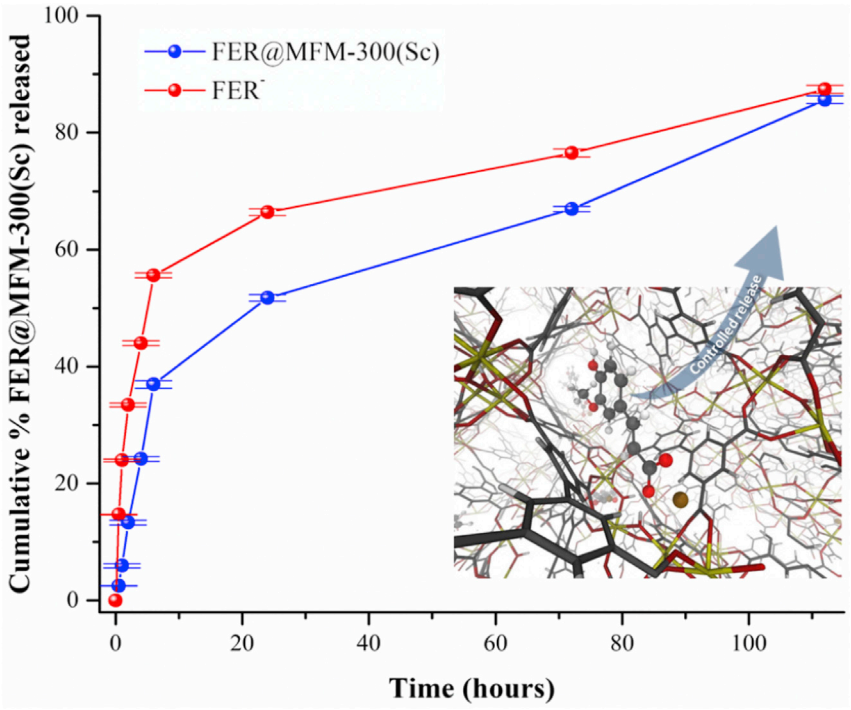

Figure 1. Controlled Release of FER in FER@MFM-300(Sc)

Comparison between the *in vitro* release profile of free FER^- (red circles) and the FER^- delivered from the MFM-300(Sc) thorough the dialysis bag technique (blue circles). Five independent *in vitro* experiments were performed to generate the error bars (statistics). Lines are shown to guide the eyes. A schematic representation of the release of FER^- from a FER@MFM-300(Sc) composite is shown as inset. See also Figures S1, S3, and S6.

diffraction analysis of the drug-loaded matrix FER@MFM-300(Sc) (ferulate is adsorbed as FER^- and Na^+) shows that the impregnation process does not modify the crystalline structure of MFM-300(Sc) (Figure S3), whereas N_2 adsorption measurements revealed a decrease of the Brunauer, Emmett and Teller (BET) area and pore volume with respect to the pristine solid (915 $m^2\ g^{-1}$ and 0.39 $cm^3\ g^{-1}$ versus 1,300 $m^2\ g^{-1}$ and 0.56 $cm^3\ g^{-1}$, respectively) (Figure S4). Grand Canonical Monte Carlo (GCMC) simulations (see Supplemental Information for details) further predicted a lower uptake of FER^- confined in the pores (10.7 wt%) associated with a decrease of the theoretical N_2-accessible surface area from the empty to the FER@MFM-300(Sc) materials (1,480 $m^2\ g^{-1}$ versus 1,290 $m^2\ g^{-1}$). This strongly suggests that part of the experimental payload is not associated with a confinement of FER^- in the pores of the MOF.

The drug-release kinetics of FER@MFM-300(Sc) was further assessed by *in vitro* studies using a dialysis bag diffusion technique (Supplemental Information). Two distinct regimes can be distinguished in the drug-release profile (Figure 1). Initially, ca. 37.0% of FER^- is released within the first 6 h; this fast initial release is associated with the well-known burst effect (Bellido et al., 2014; Li et al., 2017; Ruyra et al., 2015; Velásquez-Hernández et al., 2019), and we can exclude that it is related to the degradation of MFM-300(Sc), since we have evidenced that the structure maintains its integrity after the drug release experiments and under the simulated physiological conditions used for the cytotoxicity assays (Supplemental Information, Figure S3). Interestingly, this payload (6.4 wt%) corresponds roughly to the deviation between the total experimental uptake and the predicted value for FER^- confined in the pores (5.4 wt%). This first regime is thus most probably assigned to the release of FER^- initially adsorbed at the external surface of the MOF. In other words, this first FER^- release does not come from the micropores of MFM-300(Sc). This most likely comes from the external surface of the MOF crystals. Conversely, in the second regime the release process is considerably slower, releasing ca. 53% of the loaded drug during further ca. 94 h, approximately 4 days. Release of 9.7 wt% (end of the experiment) is in good agreement with the 10.7 wt% predicted by our calculations, supporting that this corresponds to the delivery of FER^- initially confined in the pores of the MOF material.

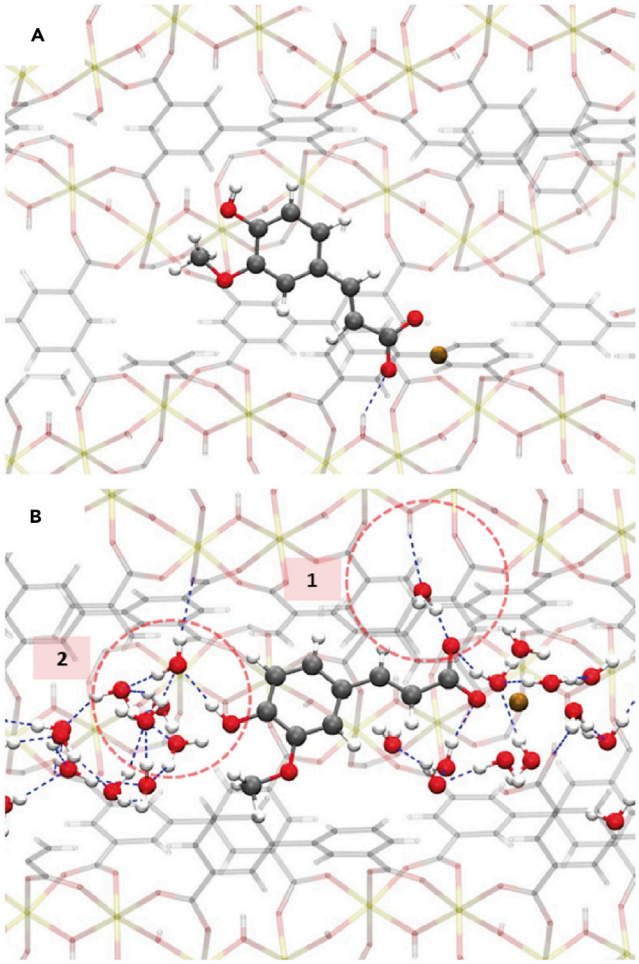

Figure 2. Microscopic Illustration of FER^- Adsorption in the MFM-300(Sc) Porosity

Representative MC snapshots of the FER^- adsorption in MFM-300(Sc) (A) at the dry state, displaying the single-adduct between the FER^- carboxylic groups and the μ-OH groups of the pore wall and (B) in solution, showing the FER^- interactions with H_2O molecules forming either (1) a single adduct with the μ-OH groups of the pore wall or (2) clusters at the center of the pore. Sc, O, C, and H are, respectively, represented in yellow, red, gray, and white. MFM-300(Sc) atoms are shown translucid for clarity. H-bonds are shown in dashed blue lines. Captions associated to the RDFs are described in the text.

See also Figures S2, S7, S13, S14, and S15.

Microscopic Understanding of the FER@MFM-300(Sc) Interactions

Monte Carlo (MC) and Density Functional Theory (DFT) calculations were further combined to understand the microscopic origin of this slow release. Analysis of the MC configurations for the adsorption of FER^- in the dry state revealed that the drug molecule establishes relatively strong hydrogen bonds with the μ-OH functional groups of MFM-300(Sc) via their carboxylic groups with characteristic O_{COO^-} - $O_{\mu\text{-}OH}$ distance of ca. 3.0 Å as seen by the corresponding radial distribution functions (RDFs) plotted in Figure S15A. Such an arrangement illustrated in Figure 2A leads to a high DFT-calculated binding energy (−43.5 kcal • mol^{-1}) that needs to be overcome in order for the molecules to be expelled from the MOF framework. Our MC simulations performed in solution further evidenced that FER^- species interact strongly with water via their carboxylic groups with characteristic short O_{COO^-} - O_W distance of 2.5 Å as seen by the corresponding RDF plotted in Figure S15B. A fraction of these water molecules equally establishes strong hydrogen bonds with the μ-OH groups of the MOF pore wall with characteristic O_w - $O_{\mu\text{-}OH}$ distance of 2.7 Å (Figure S15B). This concerted FER^- water and water-MOF interaction scenario offers an optimal scenario to stabilize FER^- species in the confined environment, water playing a pivotal role by acting as a bridge between the MOF pore-wall and FER^- to retain strongly the drug as can be seen in Figure 2B. One can also notice that besides

forming a strong hydrogen bond network, as seen by the high intensity of the peak at 2.8 Å in the RDF corresponding to the O_w – O_w pairs (Figure S15B), the water molecules form side interactions with the other functional groups of FER^- (Figures 2B and S15B). DFT simulations further confirmed that such an arrangement of FER^- is highly stabilized with a corresponding binding energy of −120 kcal • mol^{-1}, consistent with a slow release observed experimentally. In line with these computational simulations, the experimental ^{13}C CP MAS spectra (Figure S7) confirm the interaction of FER^- within the MOF material. In the spectrum of FER@MFM-300(Sc), the NMR signals originating from FER^- are considerably lower in comparison with those for MFM-300(Sc). Two signals are observed in the carboxylate region; the first one at 174.9 ppm is the most intense and is attributable to COO^- bonded to Sc^{+3} in MFM-300(Sc). The second one appears at 170.7 ppm and is attributable to COO^- coming from the FER^- species. The signal of COO^- $FER^-\cdots Na^+$ appears at 173.1 ppm, i.e., that COO^- shifted 2.4 ppm to stronger fields when adsorbed in MFM-300(Sc) (Figure S7).

Indeed, the drug adsorption profile accomplishes the desired drug-delivery kinetic for transdermal drug administration applications, where the drug carrier systems are designed normally to release the cargo within 1–7 days.

Cytotoxicity Experiments

Accordingly, the cytotoxicity of MFM-300(Sc) and its components ($BPTC^{-4}$, Sc^{+3}) were investigated separately, monitoring their impact in the cell viability and proliferation of human dermal fibroblasts (Supplemental Information) (Kalpana et al., 2010). Five different concentration solutions (5, 25, 100, 250, and 500 ppm) of $BPTC^{-4}$, Sc^{+3}, and MFM-300(Sc) were tested (Supplemental Information). The collected data revealed that both MFM-300(Sc) and Sc^{+3} did not considerably affect the cell viability, in comparison with positive controls. More than 98% of the cells remain viable after 24 h of incubation at any of the concentrations employed (Figures 3 and S9). This behavior remained almost constant even after 120 h. However, the culture well plates pre-treated with $BPTC^{-4}$ presented a considerable reduction of cell viability in a dose-dependent way. Since some cells separate from the culture plate when they are not viable, the number of cells was also assessed. The cells treated with MFM-300(Sc) only showed an 80% reduction of the number of live cells at 500 ppm. Cells treated with Sc^{+3} showed a 120% reduction at 25–500 ppm. Treatments with $BPTC^{-4}$ decrease considerably the number of cells from 5.5 times at 5 ppm to 8.8 times at 500 ppm. Moreover, the cell images collected on an epifluorescence microscope showed that, even when using only 5 ppm of $BPTC^{-4}$, in the incubation media, the cells adopt a rounded morphology. This last observation indicates that the fibroblast attachment was not appropriate on the culture wells pre-treated with $BPTC^{-4}$ (Figures 3 and S9). These results not only demonstrate that Sc^{+3} and MFM-300(Sc) exhibit an acceptable biocompatibility for topical drug administration but also confirm that $BPTC^{-4}$ shows a negative cytotoxic effect.

These findings encouraged us to investigate the transdermal permeability of FER^- upon the topical administration of this antioxidant using FER@MFM-300(Sc) as a drug carrier. An active ingredient will exert its effect on its therapeutic target by releasing it from its pharmaceutical form, and it will subsequently arrive at its site of action.

Evaluation of the Antioxidant Effect of FER^- Released from the MFM-300(Sc) Matrix

The *ex vivo* permeation assays were carried out on Franz diffusion cells using low back human tissue (Figures 4A and S10). This tissue was obtained from a female donor, who underwent aesthetic surgery, and it was employed with the prior consent of the donor (Supplemental Information, Figure S10). The Franz chambers consist of two compartments (donor and receptor) separated by the skin membrane (Figure 4A). The skin was placed in the donor compartment, where the *stratum corneum* (SC) was exposed to a suspension of FER@MFM-300(Sc) (41.4 mg mL^{-1}) (Figures 4B and S10). The receptor compartment was filled with PBS (phosphate-buffered saline) at 37°C and kept under stirring (500 rpm) for 87 h. Afterward, the receptor medium was sampled to determine the amount of antioxidant diffused across the skin barrier (referred as systemic diffusion). As a control test, this permeation experiment was also performed using an aqueous suspension of FA (6.68 mg mL^{-1}) (Figure 4C). Then, once completed the permeation assay, the skin samples were further analyzed to determine the biodistribution of the antioxidant within the skin layers. The tape stripping technique was employed to remove the SC layer of each skin sample (Binder et al., 2019; Escobar-Chávez et al., 2008; Esposito et al., 2018; Limcharoen et al., 2019). Then, these tape stripping samples and the remaining part of each skin sample were analyzed to estimate the amount of the antioxidant retained in the SC and in the inner layers of the skin. The data collected show that, when using the FER@MFM-300(Sc) system, ca. 10.40% of the cargo permeates through the skin to the

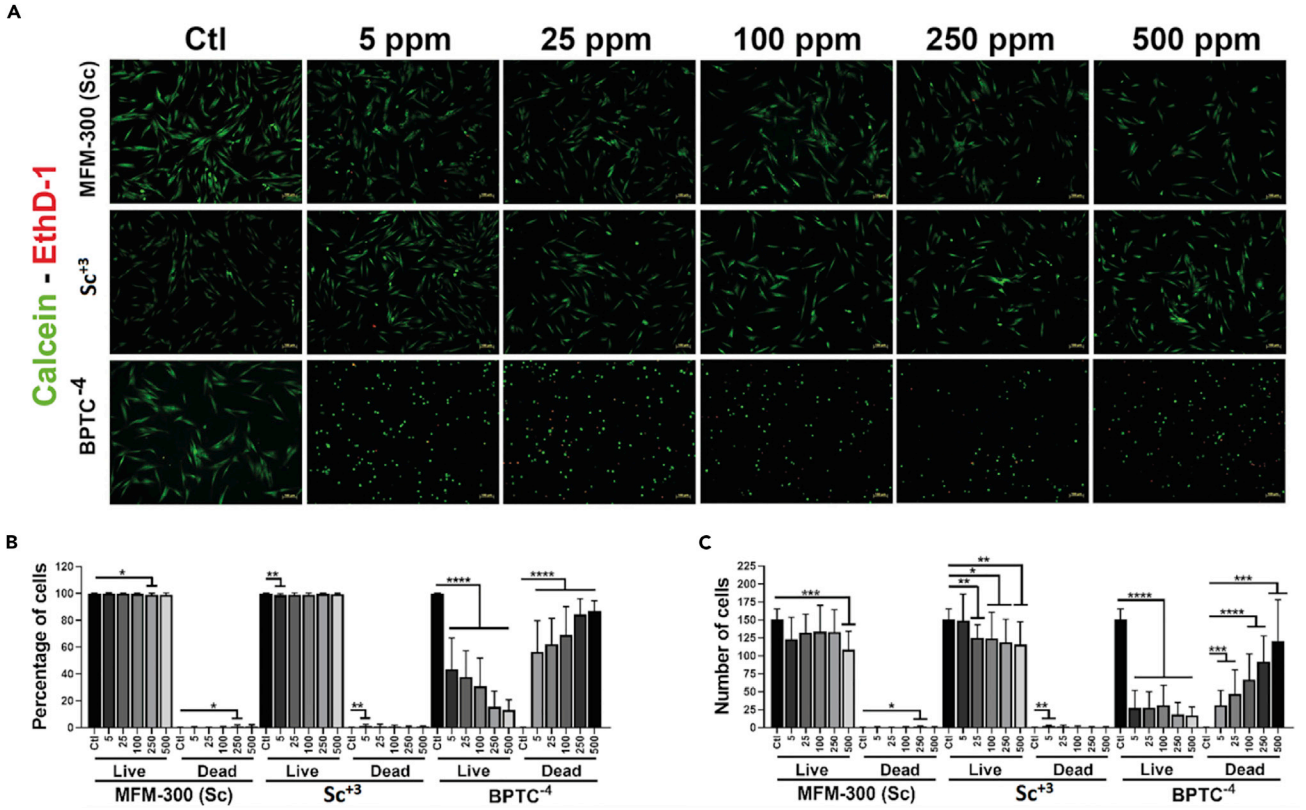

Figure 3. Cytotoxicity Experiments of MFM-300(Sc), Sc^{+3}, and $BPTC^{-4}$

(A) Viable (green/calcein positives) and dead (red/EthD-1 positives) cells seeded on culture well plates pre-treated with different concentrations of MFM-300(Sc), Sc(III) and $BPTC^{-4}$.

(B) Viable cell percentage and (C) total number of viable cells. ANOVA test and Sidak's multiple comparisons test. *$p < 0.05$, **$p < 0.005$, ***$p < 0.0005$ and ****$p < 0.00005$. Scale bars correspond to 100 μm.

See also Figures S9 and S12.

systemic compartment, whereas in the system with an aqueous suspension of free FA only ca. 5.71% of the drug reaches the receptor compartment (Figures 4B and 4C), presumably because of oxidation and poor solubility of free FA in the skin. Interestingly, the amount of the antioxidant retained in the SC when using the FER@MFM-300(Sc) formulation and free FA is comparable ca. 0.20% and almost negligible, respectively. The carrier (MFM-300(Sc)) was retained in the SC as demonstrated by the size of the crystals (Figure S8). In addition, the quantity of the drug retained in the dermal and epidermal layers is around 0.29% when using FER@MFM-300(Sc) and 0.39% in the case of free FA. The permeation fluxes determined for FER^- and FER@MFM-300(Sc) were 12.1×10^{-4} and 5.9×10^{-4} ($nmol \cdot cm^{-2} \cdot h^{-1}$), respectively. These findings demonstrate that our carrier material (MFM-300(Sc)) improves the permeation of the drug through the human skin, in comparison with the free FA. Such differences might be attributed to the promotion in the absorption of FER^- inside FER@MFM-300(Sc) possibly by transcellular or paracellular routes. In addition, there is a higher availability of the drug when it is administrated as the ion FER^- species than when it is administrated directly as the protonated species (FA).

Thus, the poor solubility of FA in the aqueous suspension, as well as its propensity to oxidize, reduces the concentration of the available molecular species retarding the permeation through the skin layers. The therapeutic reach of the permeation of FER^- from FER@MFM-300(Sc) in the epidermis-dermis region, systemic, or deposition from the SC, also implies the subsequent prolonged release for up to 5 days of the cargo with the innocuous biodegradation of the carrier, a requirement of special interest for chronic clinical conditions.

Evidence of non-permeation of FER@MFM-300(Sc) was recorded by SEM studies before and after the tape stripping technique owing to the particle size of FER@MFM-300(Sc) (5×13 μm), which corroborates the new system as only for modified release and not for permeation (Figure S11). It is worth to emphasize

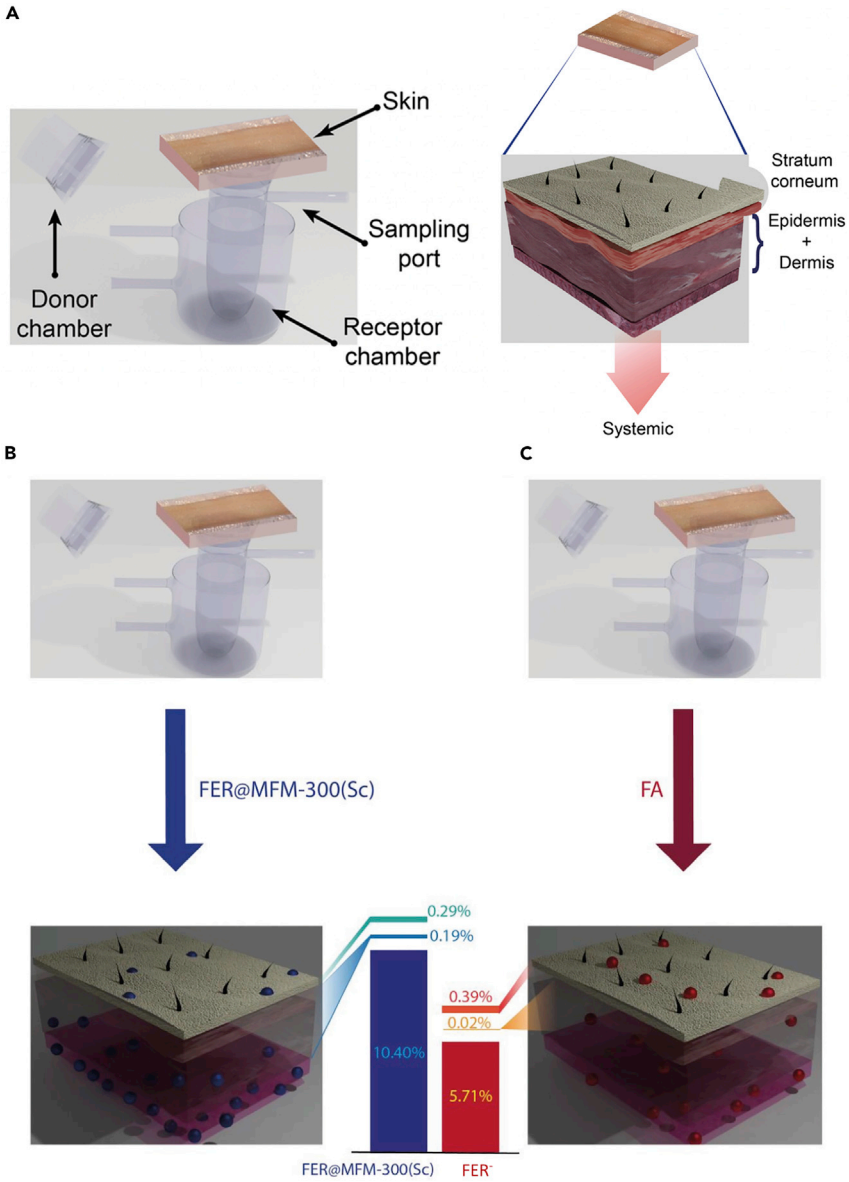

Figure 4. *Ex Vivo* Permeation Experiments of Free and Entrapped FER⁻

(A–C) (A) Structural design of a Franz diffusion cell and schematic representation of the skin layers; (B) *ex vivo* permeation experiments of FER⁻ using the FER@MFM-300(Sc) formulation, and amount of antioxidant (%) retained within the skin and released in the receptor chamber (systemic); and (C) *ex vivo* permeation experiments using an aqueous suspension of free FA and percentage of antioxidant retained within the skin and released in the receptor chamber (systemic).
See also Figures S8, S10, and S11.

that, for this model with real human skin, we did not perform more repetition experiments to achieve a certain level of statistics because of the limitations of achieving reproducible samples (same origin of the human skin: ideally same patient, same area of extraction, age of the donor, sex, ethnicity, etc.). More than focusing on the absolute permeation values of FER⁻, it is very significant the trends that we show.

Finally, to examine if the therapeutic drug preserved its antioxidant pharmacological effects after the long-term release process, the antioxidant efficacy, of FER⁻ released from the microporous carrier (MFM-300(Sc)), was tested by monitoring the reactive oxygen species (ROS) produced in dermal skin fibroblasts upon being treated with H_2O_2. First, the release of the antioxidant was performed by soaking the MOF

composite (FER@MFM-300(Sc)) in the cell culture media for 5 days. Then, the fibroblasts were pre-treated with this incubation media for 20 min. Subsequently, the cells were exposed to H_2O_2 for 20 min to induce the oxidative stress. The efficacy of the antioxidant in protecting skin fibroblasts from H_2O_2-induced ROS toxicity was determined using CellRox flow cytometry assay (see Supplemental Information, Figure S9). The results obtained demonstrated that the unstained condition marks 100% of cells without ROS expression (CellRox+), dead cells (7-AAD+), or doubly marked (CellRox/7-AAD+). In the basal state (without H_2O_2 treatment), only 0.2% of the cells remain unlabeled and 67.5% show ROS expression, whereas, as expected, the cells incubated with H_2O_2 present an increase in ROS production (88.7%), the unlabeled population decreases (0.6%), and the population with dead cells and ROS + showed 10.7%. However, when the cells were treated with FER@MFM-300(Sc) (100 ppm) the percentage of unstained cells (without ROS or dead cell staining) increase considerably (25.9%) in comparison with the values observed in the basal state (0.6%). This fact confirms that the FER^- released from FER@MFM-300(Sc) maintains its bio-functionality by scavenging ROS species. Another result shows that only the application of the MFM-300(Sc) to the cells increase the unlabeled cells from 0.6% to 1.3%, suggesting that the MFM-300(Sc) exhibits an unexpected antioxidant capacity. These findings suggest that FER@MFM-300(Sc) not only allows the long-term sustained release of FER^- but also enhances the bio-preservation of dermal skin fibroblasts during the delivery process.

In summary, this work demonstrates that MFM-300(Sc) is an efficient drug carrier by virtue of its excellent biocompatibility in human skin cells, remarkable stability under physiological conditions, and adequate controlled release for topical applications. The incorporation of FER^- into MFM-300(Sc), in comparison with other well-known or even commercial materials like hydrotalcites (Lima et al., 2013), provided a longer-term controlled release through human skin. MFM-300(Sc) also demonstrated a higher chemical stability in comparison with typical MOF DDSs like MIL-100 and MIL-101(Horcajada et al., 2006; Li et al., 2017). This particular chemical stability for MFM-300(Sc) provides a benchmark material for future investigations in order to compare with other MOF carries, particularly those constructed with Sc(III) metal centers. In addition, our study reveals that this material improves the systemic delivery of ferulate leading to the controlled and sustained long-term delivery of the cargo, which avoids both the degradation of ferulate, and the continuous re-application of the drug during, relatively, a long time. These findings pave the way toward the extended use of Sc(III)-based MOFs as drug carriers.

Limitations of the Study

In this study, the topical drug bioavailability was assessed by *in vitro* experiments using a two-chamber Franz cell. The main disadvantage of this system is that it does not consider the *in vivo* skin processes and does not mimic accurately the living state of the skin. For instance, the skin normally functions under air from the environment. However, during the permeation studies, SC is typically exposed to wet conditions for prolonged periods. On the other hand, the current work was limited to the release of FER^-. Future efforts should test other drugs in order to drive the extended use of Sc(III)-based MOFs as drug carriers.

Resource Availability

Lead Contact

Further information and requests for resources and reagents should be directed to and will be fulfilled by the Lead Contact, Ilich A. Ibarra (argel@unam.mx).

Materials Availability

This study did not generate new unique reagents.

Data and Code Availability

All the data needed to evaluate the conclusions of this work are detailed in the main text and/or the Supplemental Information. Additional data related to this paper may be requested from Ilich A. Ibarra (argel@unam.mx).

METHODS

All methods can be found in the accompanying Transparent Methods supplemental file.

SUPPLEMENTAL INFORMATION

Supplemental Information can be found online at https://doi.org/10.1016/j.isci.2020.101156.

ACKNOWLEDGMENTS

The authors thank Dr. A. Tejeda-Cruz (powder X-ray; IIM-UNAM) and PAPIIT UNAM (IN202820), Mexico for financial support. E.L. thanks PAPIIT UNAM (IN205320), Mexico for financial support. G.L-G. thanks PAPIIT UNAM (TA200318) and CONACYT (CB-A1-S-15759), Mexico for financial support. R.S.-S. thanks CONACyT (B-S-40505), Mexico for financial support. M.J.V.-H. thanks CONACyT (419210), Mexico for the postdoctoral scholarship. Thanks to U. Winnberg (ITAM) for scientific discussions and G. Ibarra-Winnberg for conceptualizing the design of this contribution.

AUTHOR CONTRIBUTIONS

G.O.-T and M.J.V.-H.: Synthesis and characterization of MFM-300(Sc), assistance of different experiments, data collecting, and integration of the full manuscript. P.G.M.M. and J.A.Z.: computational calculations. J.A.-R., G.L.-G., and J.J.M.: *ex vivo* experiments. R.S.-S. and M.A.P.-D.: *in vitro* experiments. I.A.L. and R.S.F.: reactive oxygen species (ROS) experiments. G.M., E.L., and I.A.I.: Principal leader investigators who conducted the entire project from the bio-compatible (E.L.), computational (G.M.) and material (I.A.I.) perspectives.

DECLARATION OF INTERESTS

The authors declare no competing interests.

Received: April 1, 2020
Revised: April 24, 2020
Accepted: May 6, 2020
Published: June 26, 2020

REFERENCES

Antolovich, M., Bedgood, D.R., Bishop, A.G., Jardine, D., Prenzler, P.D., and Robards, K. (2004). LC-MS investigation of oxidation products of phenolic antioxidants. J. Agric. Food Chem. *52*, 962–971.

Bellido, E., Guillevic, M., Hidalgo, T., Santander-Ortega, M.J., Serre, C., and Horcajada, P. (2014). Understanding the colloidal stability of the mesoporous MIL-100(Fe) nanoparticles in physiological media. Langmuir *30*, 5911–5920.

Binder, L., Mazál, J., Petz, R., Klang, V., and Valenta, C. (2019). The role of viscosity on skin penetration from cellulose ether-based hydrogels. Ski. Res. Technol. *25*, 725–734.

Chen, W., and Wu, C. (2018). Synthesis, functionalization, and applications of metal-organic frameworks in biomedicine. Dalton Trans. *47*, 2114–2133.

Chen, B., Xiang, S., and Qian, G. (2010a). Metal-organic frameworks with functional pores for recognition of small molecules. Acc. Chem. Res. *43*, 1115–1124.

Chen, M., Liu, X., and Fahr, A. (2010b). Skin delivery of ferulic acid from different vesicular systems. J. Biomed. Nanotechnol. *6*, 577–585.

Chen, Y., Li, P., Modica, J.A., Drout, R.J., and Farha, O.K. (2018). Acid-resistant mesoporous metal-organic framework toward oral insulin delivery: protein encapsulation, protection, and release. J. Am. Chem. Soc. *140*, 5678–5681.

Cui, Y., Yue, Y., Qian, G., and Chen, B. (2012). Luminescent functional metal-organic frameworks. Chem. Rev. *112*, 1126–1162.

Doonan, C., Riccò, R., Liang, K., Bradshaw, D., and Falcaro, P. (2017). Metal-organic frameworks at the biointerface: synthetic strategies and applications. Acc. Chem. Res. *50*, 1423–1432.

Escobar-Chávez, J.J., Merino-Sanjuán, V., López-Cervantes, M., Urban-Morlan, Z., Piñón-Segundo, E., Quintanar-Guerrero, D., and Ganem-Quintanar, A. (2008). The tape-stripping technique as a method for drug quantification in skin. J. Pharm. Pharm. Sci. *11*, 104–130.

Esposito, E., Carducci, F., Mariani, P., Huang, N., Simelière, F., Cortesi, R., Romeo, G., and Puglia, C. (2018). Monoolein liquid crystalline phases for topical delivery of crocetin. Colloids Surf. B Biointerfaces *171*, 67–74.

Ford-Hutchinson, A.W., and Perkins, D.J. (1971). The binding of scandium ions to transferrin in vivo and in vitro. Eur. J. Biochem. *21*, 55–59.

Furukawa, H., Cordova, K.E., O'Keeffe, M., and Yaghi, O.M. (2013). The chemistry and applications of metal-organic frameworks. Am. Assoc. Adv. Sci. *341*, 974.

Gillies, E.R., and Fréchet, J.M.J. (2005). Dendrimers and dendritic polymers in drug delivery. Drug Discov. Today *10*, 35–43.

Giménez-Marqués, M., Hidalgo, T., Serre, C., and Horcajada, P. (2016). Nanostructured metal-organic frameworks and their bio-related applications. Coord. Chem. Rev. *307*, 342–360.

Horcajada, P., Serre, C., Vallet-Regí, M., Sebban, M., Taulelle, F., and Férey, G. (2006). Metal-organic frameworks as efficient materials for drug delivery. Angew. Chem. Int. Ed. *45*, 5974–5978.

Horcajada, P., Chalati, T., Serre, C., Gillet, B., Sebrie, C., Baati, T., Eubank, J.F., Heurtaux, D., Clayette, P., Kreuz, C., et al. (2010). Porous metal-organic-framework nanoscale carriers as a potential platform for drug deliveryand imaging. Nat. Mater. *9*, 172–178.

Horcajada, P., Gref, R., Baati, T., Allan, P.K., Maurin, G., Couvreur, P., Férey, G., Morris, R.E., and Serre, C. (2012). Metal-organic frameworks in biomedicine. Chem. Rev. *112*, 1232–1268.

Horovitz, C.T. (2012). Biochemistry of Scandium and Yttrium, Part 1: Physical and Chemical Fundamentals (Springer Science & Business Media).

Ibarra, I.A., Yang, S., Lin, X., Blake, A.J., Rizkallah, P.J., Nowell, H., Allan, D.R., Champness, N.R., Hubberstey, P., and Schröder, M. (2011). Highly porous and robust scandium-based metal-organic frameworks for hydrogen storage. Chem. Commun. *47*, 8304–8306.

Jiang, J., Zhao, Y., and Yaghi, O.M. (2016). Covalent chemistry beyond molecules. J. Am. Chem. Soc. *138*, 3255–3265.

Jie, Y., and Ying-Wei, Y. (2020). Metal-organic frameworks for biomedical applications. Small *16*, 1.

Kalpana, S.P., Mikolaj, M., Courtney, L.S., Nicole, K.B., Priyanka, G., and Audra, L.S. (2010). Challenges and opportunities in dermal/transdermal delivery. Ther. Deliv. *11*, 109–131.

Kawai, K., Wang, G., Okamoto, S., and Ochi, K. (2007). The rare earth, scandium, causes antibiotic overproduction in Streptomyces spp. FEMS Microbiol. Lett. *274*, 311–315.

Kitagawa, S., Kitaura, R., and Noro, S.I. (2004). Functional porous coordination polymers. Angew. Chem. Int. Ed. *43*, 2334–2375.

Kreno, L.E., Leong, K., Farha, O.K., Allendorf, M., Van Duyne, R.P., and Hupp, J.T. (2012). Metal-organic framework materials as chemical sensors. Chem. Rev. *112*, 1105–1125.

Li, J.R., Sculley, J., and Zhou, H.C. (2012). Metal-organic frameworks for separations. Chem. Rev. *112*, 869–932.

Li, X., Lachmanski, L., Safi, S., Sene, S., Serre, C., Grenèche, J.M., Zhang, J., and Gref, R. (2017). New insights into the degradation mechanism of metal-organic frameworks drug carriers. Sci. Rep. *7*, 1–11.

Liang, K., Ricco, R., Doherty, C.M., Styles, M.J., Bell, S., Kirby, N., Mudie, S., Haylock, D., Hill, A.J., Doonan, C.J., et al. (2015). Biomimetic mineralization of metal-organic frameworks as protective coatings for biomacromolecules. Nat. Commun. *6*, 4–11.

Liang, W., Xu, H., Carraro, F., Maddigan, N.K., Li, Q., Bell, S.G., Huang, D.M., Tarzia, A., Solomon, M.B., Amenitsch, H., et al. (2019). Enhanced activity of enzymes encapsulated in hydrophilic metal-organic frameworks. J. Am. Chem. Soc. *141*, 2348–2355.

Lima, E., Flores, J., Cruz, A.S., Leyva-Gómez, G., and Krötzsch, E. (2013). Controlled release of ferulic acid from a hybrid hydrotalcite and its application as an antioxidant for human fibroblasts. Microporous Mesoporous Mater. *181*, 1–7.

Limcharoen, B., Toprangkobsin, P., Banlunara, W., Wanichwecharungruang, S., Richter, H., Lademann, J., and Patzelt, A. (2019). Increasing the percutaneous absorption and follicular penetration of retinal by topical application of proretinal nanoparticles. Eur. J. Pharm. Biopharm. *139*, 93–100.

Liu, W., Pan, Y., Xiao, W., Xu, H., Liu, D., Ren, F., Peng, X., and Liu, J. (2019). Recent developments on zinc (ii) metal-organic framework nanocarriers for physiological pH-responsive drug delivery. Medchemcomm *10*, 2038–2051.

Luo, Z., Fan, S., Gu, C., Liu, W., Chen, J., Li, B., and Liu, J. (2019). Metal–organic framework (MOF)-based nanomaterials for biomedical applications. Curr. Med. Chem. *26*, 3341–3369.

Makal, T.A., Li, J.R., Lu, W., and Zhou, H.C. (2012). Methane storage in advanced porous materials. Chem. Soc. Rev. *41*, 7761–7779.

Murray, L.J., Dinc, M., and Long, J.R. (2009). Hydrogen storage in metal-organic frameworks. Chem. Soc. Rev. *38*, 1294–1314.

Pegoraro, C., MacNeil, S., and Battaglia, G. (2012). Transdermal drug delivery: from micro to nano. Nanoscale *4*, 1881–1894.

Porter, C.J.H., Trevaskis, N.L., and Charman, W.N. (2007). Lipids and lipid-based formulations: optimizing the oral delivery of lipophilic drugs. Nat. Rev. Drug Discov. *6*, 231–248.

Ruyra, A., Yazdi, A., Espín, J., Carné-Sánchez, A., Roher, N., Lorenzo, J., Imaz, I., and Maspoch, D. (2015). Synthesis, culture medium stability, and in vitro and in vivo zebrafish embryo toxicity of metal-organic framework nanoparticles. Chemistry *21*, 2508–2518.

Sánchez-González, C., López-Chaves, C., Rivas-García, L., Galindo, P., Gómez-Aracena, J., Aranda, P., and Llopis, J. (2013). Accumulation of scandium in plasma in patients with chronic renal failure. Sci. World J. *2013*, 782745.

Senapati, S., Mahanta, A.K., Kumar, S., and Maiti, P. (2018). Controlled drug delivery vehicles for cancer treatment and their performance. Signal Transduct. Target. Ther. *3*, 1–19.

Sheberla, D., Sun, L., Blood-Forsythe, M.A., Er, S., Wade, C.R., Brozek, C.K., Aspuru-Guzik, A., and Dincă, M. (2014). High electrical conductivity in Ni3(2,3,6,7,10,11- hexaiminotriphenylene)2, a semiconducting metal-organic graphene analogue. J. Am. Chem. Soc. *136*, 8859–8862.

Sheberla, D., Bachman, J.C., Elias, J.S., Sun, C.J., Shao-Horn, Y., and Dincă, M. (2017). Conductive MOF electrodes for stable supercapacitors with high areal capacitance. Nat. Mater. *16*, 220–224.

Simon-Yarza, T., Mielcarek, A., Couvreur, P., and Serre, C. (2018). Nanoparticles of metal-organic frameworks: on the road to in vivo efficacy in biomedicine. Adv. Mater. *30*, 1.

Suh, M.P., Park, H.J., Prasad, T.K., and Lim, D.W. (2012). Hydrogen storage in metal-organic frameworks. Chem. Rev. *112*, 782–835.

Sumida, K., Rogow, D.L., Mason, J.A., Mcdonald, T.M., Bloch, E.D., Herm, Z.R., Bae, T., and Long, R. (2012). Chem. Rev. *112*, 724–781.

Szkliniarz, K., Sitarz, M., Walczak, R., Jastrzębski, J., Bilewicz, A., Choiński, J., Jakubowski, A., Majkowska, A., Stolarz, A., Trzcińska, A., et al. (2016). Production of medical Sc radioisotopes with an alpha particle beam. Appl. Radiat. Isot. *118*, 182–189.

Tchalala, M.R., Bhatt, P.M., Chappanda, K.N., Tavares, S.R., Adil, K., Belmabkhout, Y., Shkurenko, A., Cadiau, A., Heymans, N., De Weireld, G., et al. (2019). Fluorinated MOF platform for selective removal and sensing of SO 2 from flue gas and air. Nat. Commun. *10*, 1–10.

Teplensky, M.H., Fantham, M., Li, P., Wang, T.C., Mehta, J.P., Young, L.J., Moghadam, P.Z., Hupp, J.T., Farha, O.K., Kaminski, C.F., et al. (2017). Temperature treatment of highly porous zirconium-containing metal-organic frameworks extends drug delivery release. J. Am. Chem. Soc. *139*, 7522–7532.

Tibbetts, I., and Kostakis, G.E. (2020). Recent bio-advances in metal-organic frameworks. Molecules *25*, 1291.

Velásquez-Hernández, M.D.J., Ricco, R., Carraro, F., Limpoco, F.T., Linares-Moreau, M., Leitner, E., Wiltsche, H., Rattenberger, J., Schröttner, H., Frühwirt, P., et al. (2019). Degradation of ZIF-8 in phosphate buffered saline media. CrystEngComm *21*, 4538–4544.

Wang, C., Sun, H., Luan, J., Jiang, Q., Tadepalli, S., Morrissey, J.J., Kharasch, E.D., and Singamaneni, S. (2018). Metal-organic framework encapsulation for biospecimen preservation. Chem. Mater. *30*, 1291–1300.

Wu, H., Gong, Q., Olson, D.H., and Li, J. (2012). Commensurate adsorption of hydrocarbons and alcohols in microporous metal organic frameworks. Chem. Rev. *112*, 836–868.

Xiao-Gang, Y., Xiao-Min, L., Zhi-Min, Z., Ying, Z., Xin-Yi, L., Lu-Fang, M., and Shuang-Quan, Z. (2019). Facile synthesis of a micro-scale MOF host-guest with long-lasting phosphorescence and enhanced optoelectronic performance. Chem. Commun. *55*, 11099–11102.

Ya-Pan, W., Jun-Wu, T., Shan, L., Bo, L., Jun, Z., Lu-Fang, M., Dong-Sheng, L., Ya-Qian, L., and Xianhui, B. (2019). Bi-Microporous metal–organic frameworks with cubane [M4(OH)4] (M=Ni, Co) clusters and pore-space partition for electrocatalytic methanol oxidation reaction. Angew. Chem. Int. Ed. *58*, 12185–12189.

Ying, Z., Yan-Jiang, W., Ning, W., Peng, Z., Hong-Ru, F., Min-Le, H., Lu-Fang, M., and Li-Ya, W. (2019). Tetraphenylethylene-decorated metal-organic frameworks as energy-transfer platform for the detection of nitro-antibiotics and white-light emission. Inorg. Chem. *58*, 12700–12706.

Zduńska, K., Dana, A., Kolodziejczak, A., and Rotsztejn, H. (2018). Antioxidant properties of ferulic acid and its possible application. Skin Pharmacol. Physiol. *31*, 332–336.

Zhang, J., and Ma, P.X. (2013). Cyclodextrin-based supramolecular systems for drug delivery: recent progress and future perspective. Adv. Drug Deliv. Rev. *65*, 1215–1233.

Zhang, Y., Wang, J., Bai, X., Jiang, T., Zhang, Q., and Wang, S. (2012). Mesoporous silica nanoparticles for increasing the oral bioavailability and permeation of poorly water soluble drugs. Mol. Pharm. *9*, 505–513.

Zih-yi, L., Chin-Hsiu, Y., Yu-Ting, L., Hsiang-Ling, S., Kai-Wen, K., Fu-Chen, L., Ciao-Ting, C., Yi-Tsen, L., Hsin-Fen, H., and Yung-Hsiang, L. (2019). The potential application of spring Sargassum glaucescens extracts in the moisture-retention of keratinocytes and dermal fibroblast regeneration after UVA-irradiation. Cosmetics *6*, 17.

iScience, Volume *23*

Supplemental Information

Controlled Transdermal Release of Antioxidant Ferulate by a Porous Sc(III) MOF

Génesis Osorio-Toribio, Miriam de J. Velásquez-Hernández, Paulo G.M. Mileo, J. Antonio Zárate, Javier Aguila-Rosas, Gerardo Leyva-Gómez, Roberto Sánchez-Sánchez, Jonathan J. Magaña, Mario Alberto Pérez-Díaz, Isabel Abánades Lázaro, Ross S. Forgan, Guillaume Maurin, Enrique Lima, and Ilich A. Ibarra

Supplemental Information

Supplemental Figures

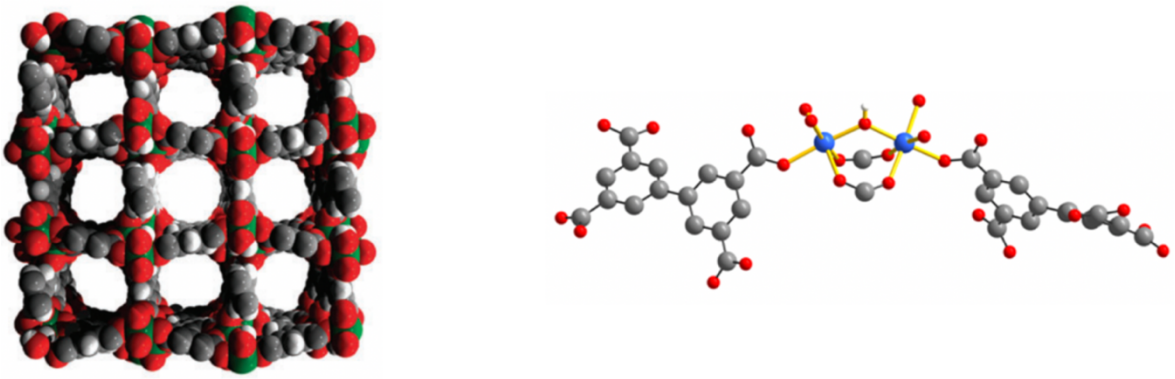

Figure S1. (left) space-filling view of the structure of MFM-300(Sc) along the b-axis showing 8.1 Å channels (Reproduced from(Ibarra et al., 2011) with permission from The Royal Society of Chemistry); and (right) view of the coordination at Sc(III) in MFM-300(Sc), showing $[BPTC]^{4-}$ and the μ_2-OH group (Reproduced from(Ibarra et al., 2016) with permission from The American Chemical Society).

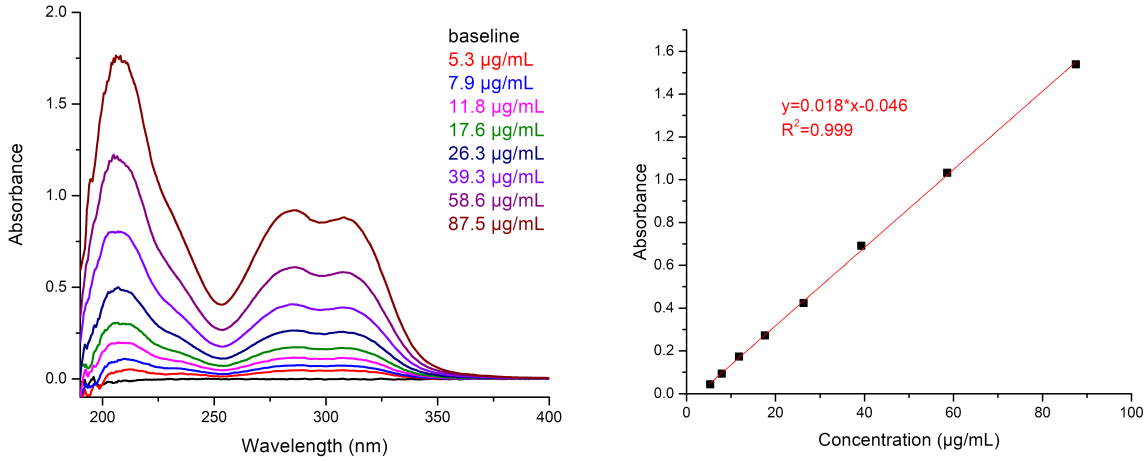

Figure S2. Drug loading quantification: (left) Absorbance scan of FER^- in 1.0 M PBS, pH=7.4 by UV-vis spectrophotometry with detection at 206 nm. Concentration range from 5.3 to 87.5 µg/mL; and (right) corresponding FER^- equation Absorbance=0.018[FER^-]-0.046 with a correlation coefficient of 0.999.

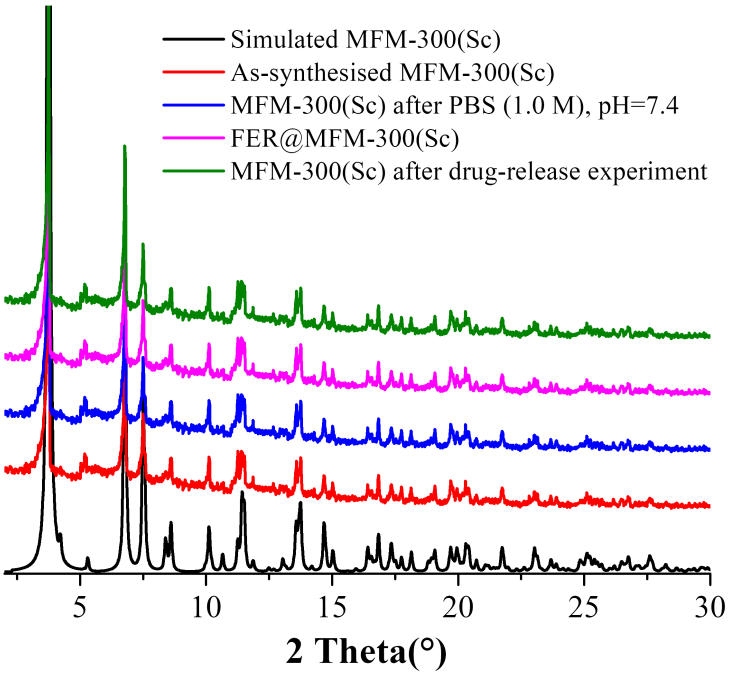

Figure S3. PXRD patterns for simulated MFM-300(Sc) (black), as-synthesised MFM-300(Sc) (red), MFM-300(Sc) after inmersion in PBS (1.0 M) for 5 dyas and pH=7.4 (blue), FER@MFM-300(Sc) (purple) and MFM-300(Sc) after drug-release experiment (green), demonstrating the structural integrety upon PBS contact for (time), upon FER-loading and release.

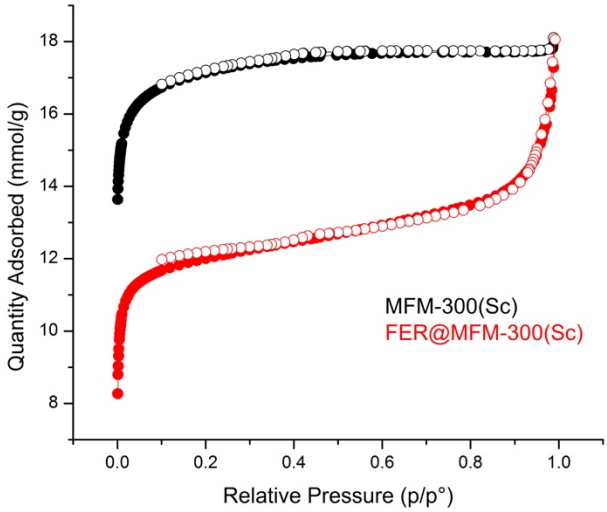

Figure S4. N_2 isotherm of MFM-300(Sc) (black) (BET area and pore volume of 1300 $m^2\ g^{-1}$ and 0.56 $cm^3\ g^{-1}$, respectively) and FER@ MFM-300(Sc) (red) (BET area and pore volume of 915 $m^2\ g^{-1}$ and 0.39 $cm^3\ g^{-1}$, respectively). Showing a decrease in posority of MFM-300(Sc) indicantes FER^- loading within the pores of the MOF material.

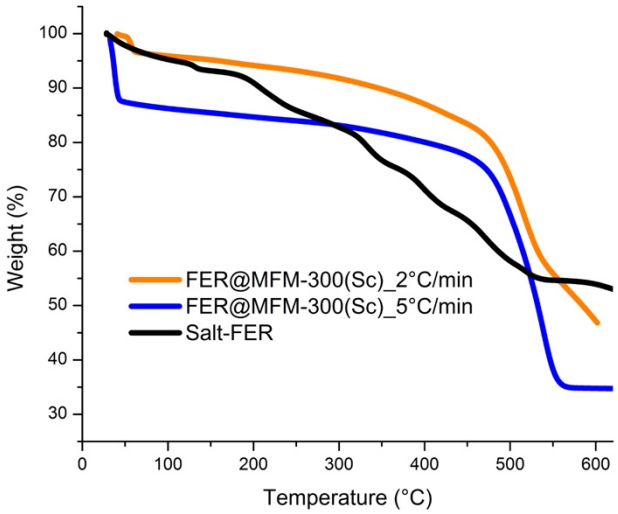

Figure S5. TGA of the as-synthesised FER@MFM-300(Sc) with a rate of 2°C/min (orange), 5°C/min (blue) and the salt of FER^- (black).

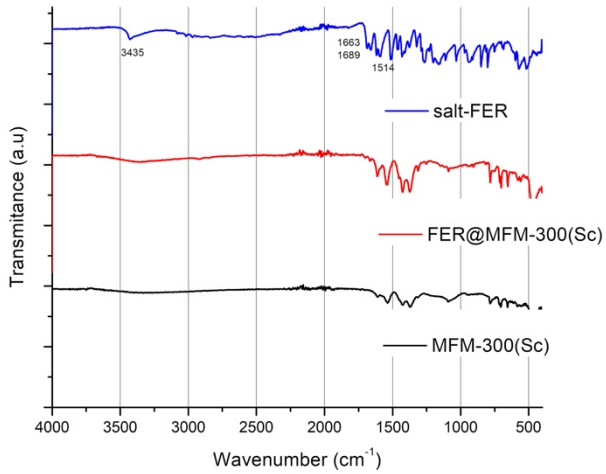

Figure S6. FTIR spectra of salt-FER has a series of peaks, such as 3435 cm^{-1} (–OH stretching), 1689 and 1663 cm^{-1} (stretching vibration of C=O groups), and 1514 cm^{-1} (C=C aromatic ring). Compared to MFM-300(Sc), the intensity around the aforementioned peaks in the FER@MFM-300 (Sc) increased, indicating that ferulic acid was grafted into the MOF.

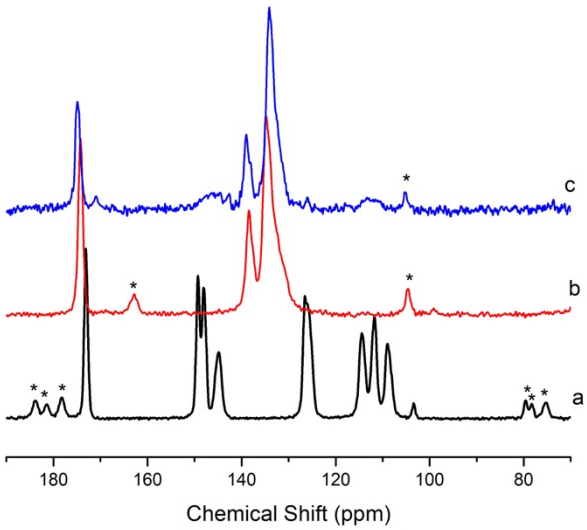

Figure S7. ^{13}C CP MAS NMR spectra of a) the $FER^{-}\cdots Na^{+}$ salt; b) MFM-300(Sc) and c) FER@MFM-300(Sc). Signals labeled * are spinning side bands.

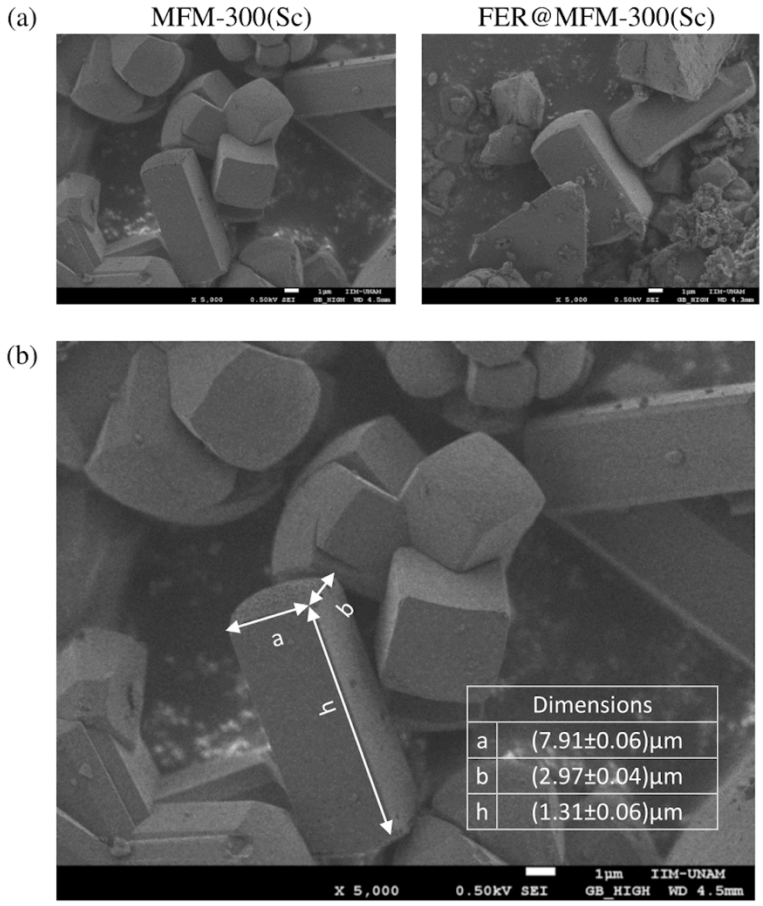

Figure S8. Scanning electron microscope images of: (a) metal-organic frameworks MFM-300(Sc) and FER@MFM-300(Sc) with 16.15 wt% of FER^{-} loading; (b) the crystal dimensions of MFM-300(Sc), magnified 5,000x.

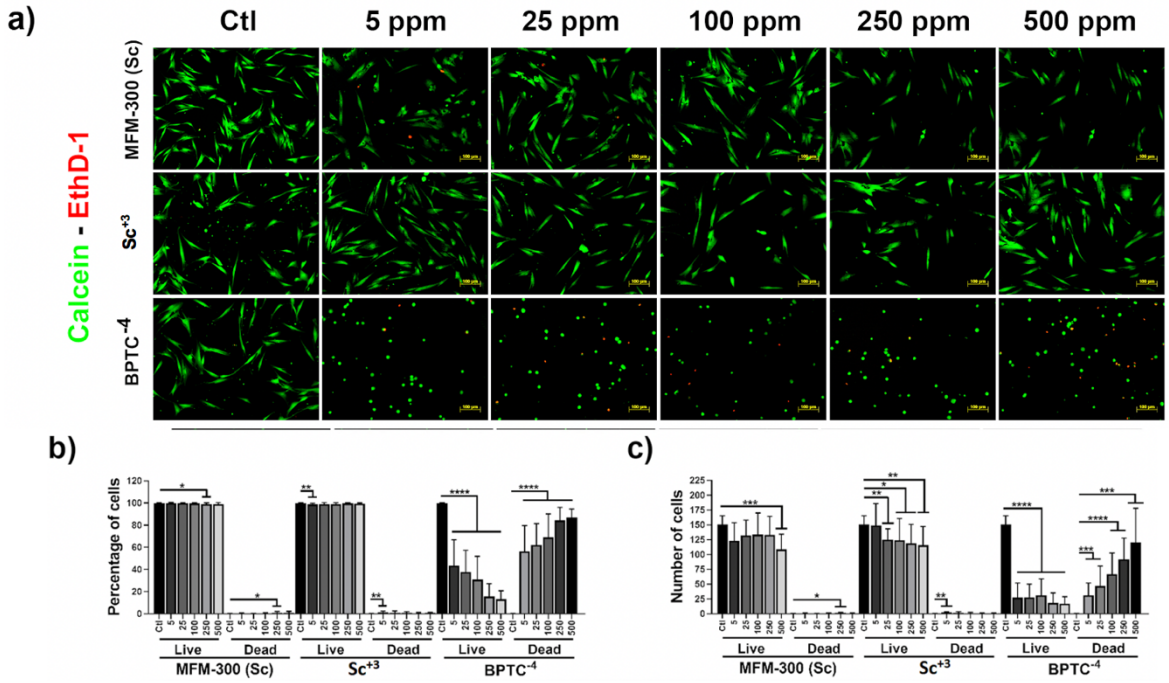

Figure S9. a) Shows viable (green/calcein positives) and dead (red/EthD-1 positives) cells seeded on culture well plates pre-treated with different concentrations of MFM-300(Sc), Sc(III) and BPTC^{-4} (20x from Figure 3). b) show the cell percentage and c) the total number of viable cells. ANOVA test and Sidak´s multiple comparisons test. *p<0.05, **p<0.005, ***p<0.0005 and ****p<0.00005. Scale bars correspond to 100 µm.

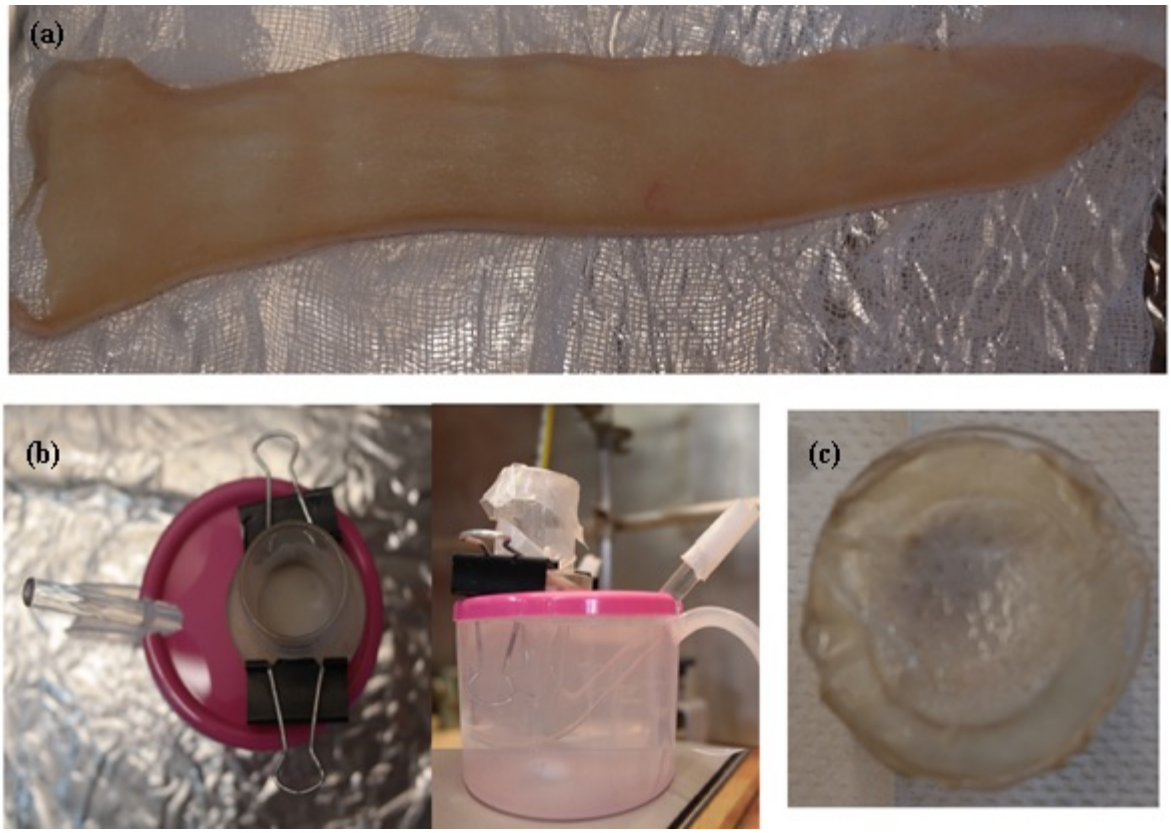

Figure S10. Franz cell images of: (a) tissue extended and pretreated for using, (b) tissue placed in customised Franz cells for diffusion studies with suspensions of FER@MFM-300(Sc) and FA; and (c) tissue after of diffusion process.

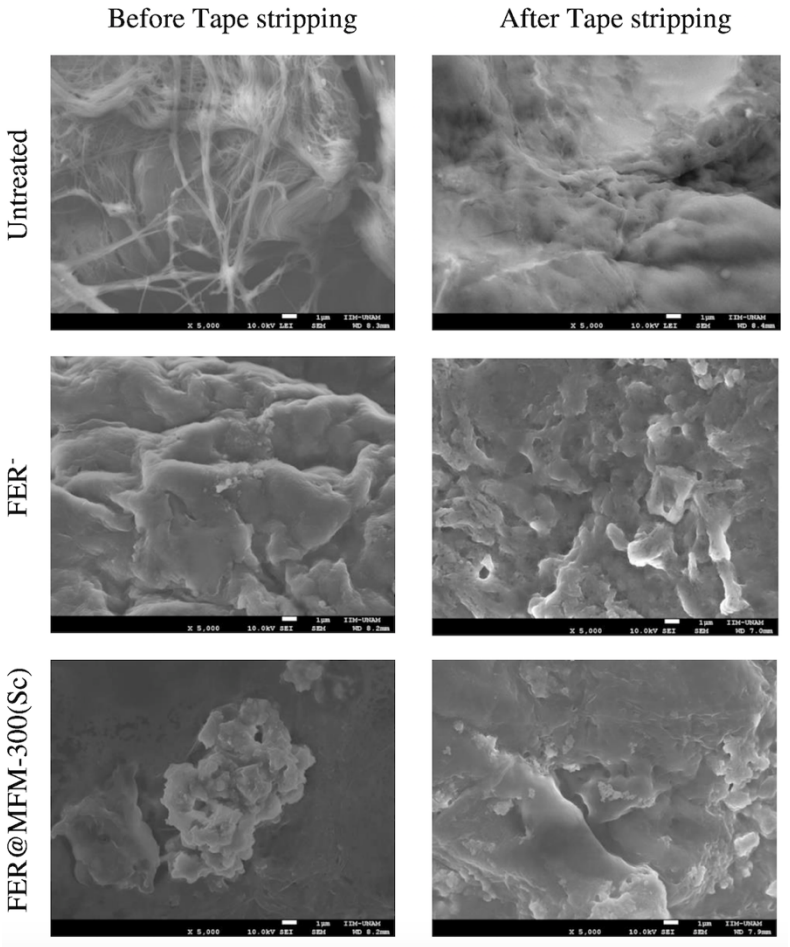

Figure S11. Scanning electron microscope images of the stratum corneum (SC) of untreated skin and treated with free and adsorbed FER^{-} in the FER@MFM-300(Sc) system, before and after the tape removal technique.

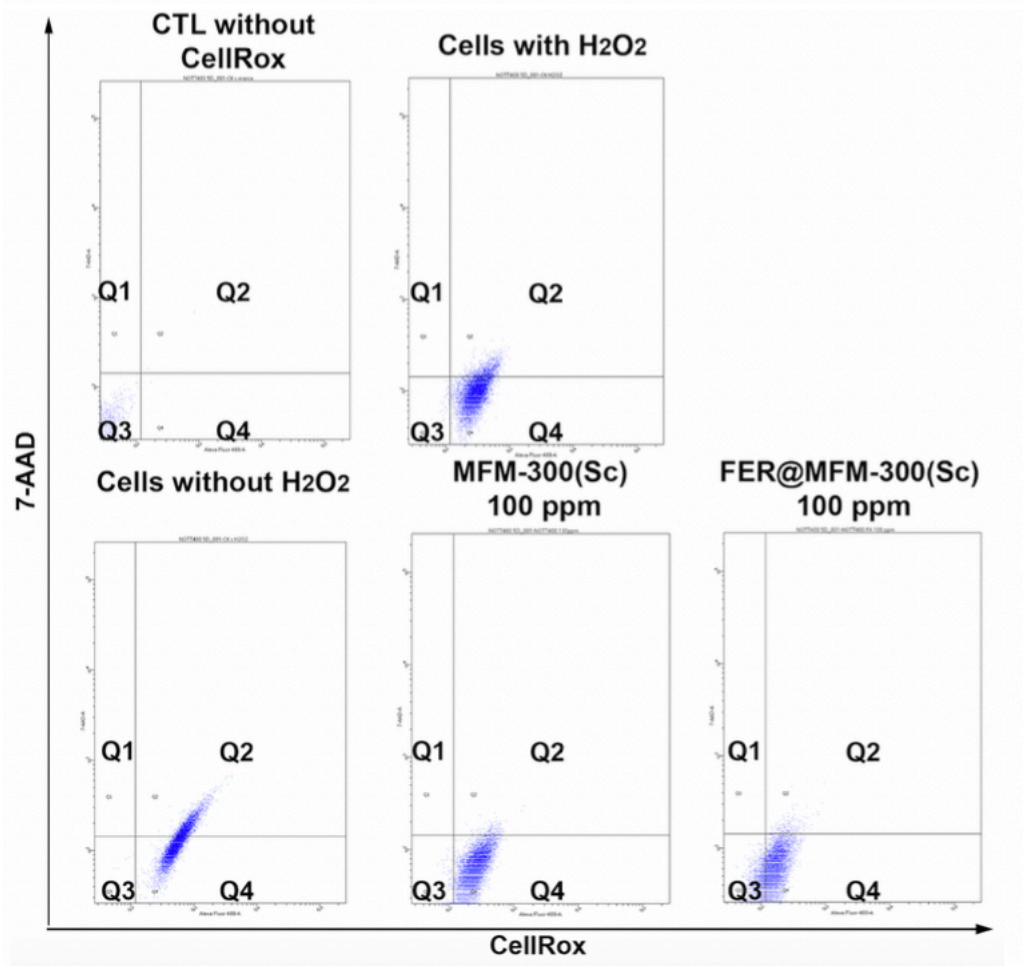

Figure S12. Flow cytometric dot plots of skin dermal fibroblasts with and without a pretreatment with a culture medium supplemented with FER@MFM-300(Sc) prior to exposure to H_2O_2. The graphs show the following populations: dead (Q1; 7-AAD), double stained (Q2; CellRox/7-AAD), not stained (Q3) and ROS positives (Q4; CellRox). All of the populations were analysed with the different experimental conditions.

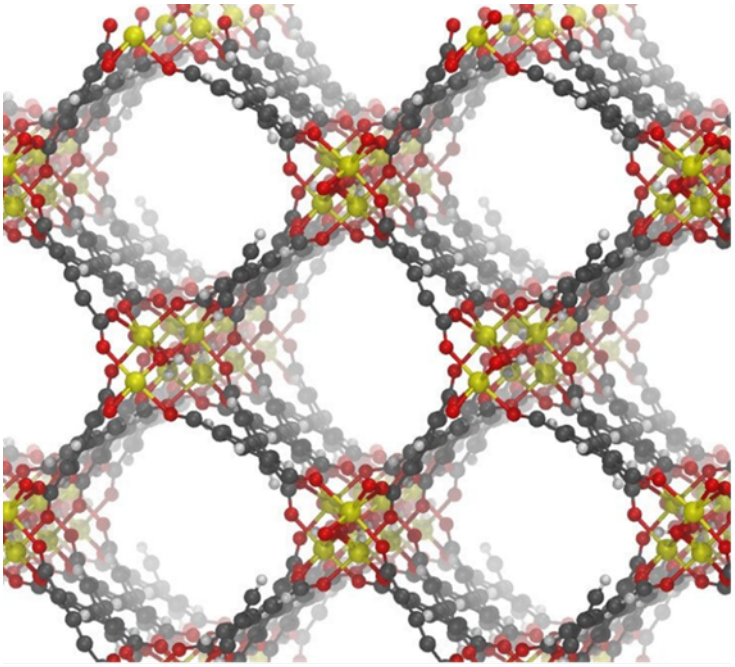

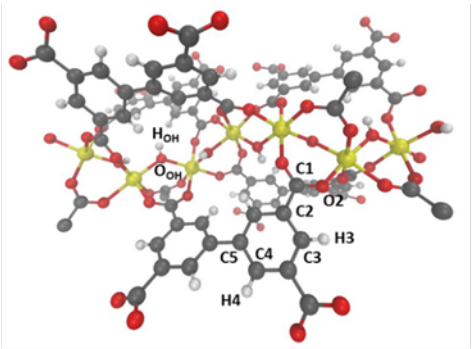

Atom type	Charge (e)
C1	0.7494
C2	-0.0288
C3	-0.1686
C4	-0.1962
C5	0.0986
O2	-0.6631
O_{OH}	-1.1049
H3	0.1219
H4	0.1960
H_{OH}	0.4475
Sc	1.8636

Figure S13. Illustration of the DFT-optimised MFM-300(Sc) structure (left), description of the different atom types (upper right) and their corresponding charges (lower right). Sc, C, O and H atoms are respectively represented in yellow, grey, red and white.

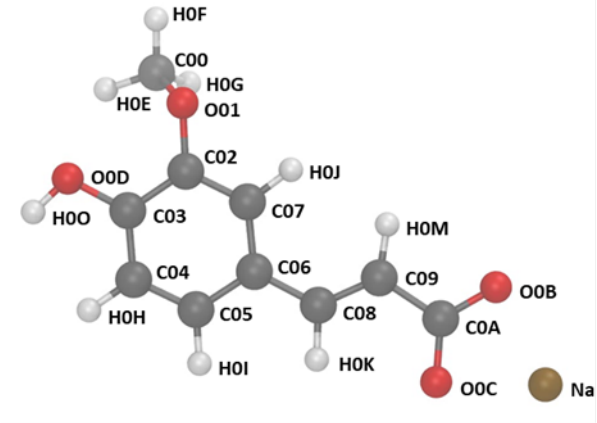

Atom type	Charge (e)	Atom type	Charge (e)
C00	-0.178	O0C	-0.753
O01	-0.285	O0D	-0.475
C02	0.237	H0E	0.083
C03	0.196	H0F	0.117
C04	-0.346	H0G	0.088
C05	-0.223	H0H	0.155
C06	0.202	H0I	0.151
C07	-0.296	H0J	0.174
C08	-0.176	H0K	0.094
C09	-0.290	H0M	0.097
C0A	0.810	H0O	0.356
O0B	-0.739	Na	1.001

Figure S14. Illustration of the Na^+ and FER^- ions showing its atom types (left) and their corresponding atom charges (right). Na, C, O and H atoms are respectively represented in ochre, grey, red and white.

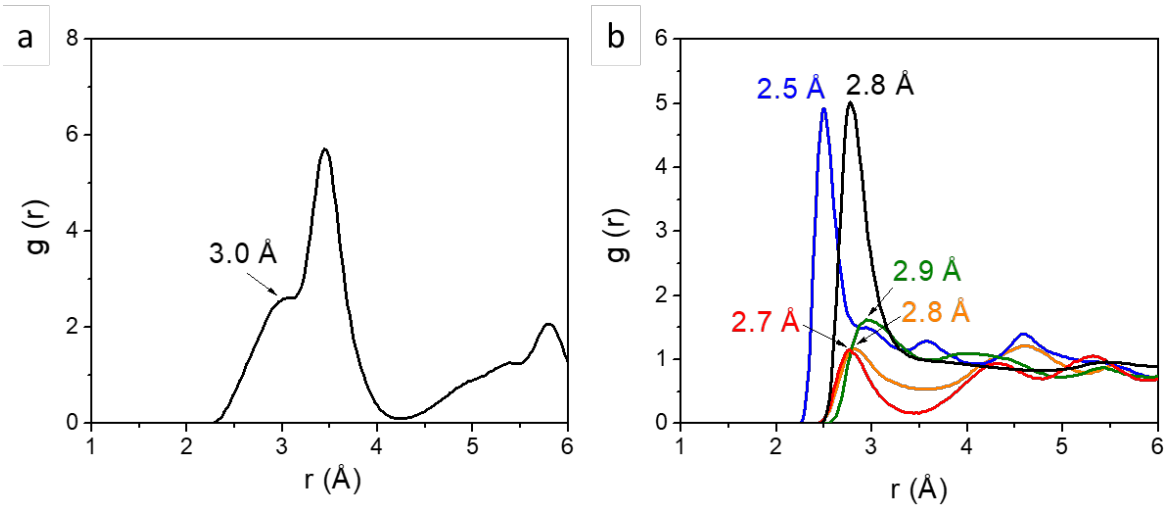

Figure S15. Radial distribution functions (RDFs) obtained from MC calculations at 310 K. (a) in the dry state, interactions between the O atoms of the COO^- functions of FER^- and the O atoms of the μ-OH groups of the MOF. (b), at the hydrated state, interactions between the oxygen atoms of the water molecules themselves (black line) and with the oxygen atoms of the μ-OH groups (red line) of MFM-300(Sc) and with the oxygen atoms of the carboxylic (blue line), ether (orange line) and phenol (green line) functional groups of FER^-.

Transparent Methods

1. Experimental

Synthesis of MFM-300(Sc)

MFM-300(Sc) ($[Sc_2(OH)_2(BPTC)]$) was synthesized according to a procedure previously reported:(Ibarra et al., 2011) Scandium triflate (0.030g, 0.061 mmol) and H_4BPTC (0.010 g, 0.030 mmol) were mixed in THF (4.0 mL), DMF (3.0 mL), water (1.0 mL) and HCl (36.5 %, 2 drops). The resultant slurry mixture was stirred until complete dissolution occurred. The solution was then placed in a pressure tube and heated in an oil bath to 75 °C for 72 h. The tube was cooled down to room temperature at a rate of 0.1 °C/min, and the colourless crystalline product was separated by filtration, washed two times with DMF (5.00 mL) and dried in air. Yield: 65.3 % (based on ligand).

Activation of MFM-300(Sc)

Acetone-exchanged (three times) samples of MFM-300(Sc) were activated at 180 °C and 1.7×10^{-3} Torr for 12 h.

Synthesis of FER@MFM-300(Sc)

FER@MFM-300(Sc) was prepared by following an impregnation protocol: 60 mg of desolvated MFM-300(Sc) (previously acetone-exchanged and activated at 180 °C and 1.7×10^{-3} Torr for 12 h. Then this activated sample was dried for 48 hours at 65° in an oven) were soaked into an aqueous solution of ferulic acid (FA) (20 mL, 0.5 mg mL^{-1}) at pH = 9 (at this pH, FA is present as an anion (analogue) ferulate (FER^-). This mixture was stirred (600 RPM) at room temperature for 5 days. Afterwards, the sample was centrifuged at 12,500 RPM for 30 minutes. The concentration of FER^- in the supernatant was analysed by UV-vis spectroscopy: The FER^- content in FER@MFM-300(Sc) was calculated by quantifying FER^- in the supernatant after centrifuging at 12,500 rpm for 30 min. The maximum absorbance peak was determined in a scan of 180 to 400 nm at a speed of 10 nm/s, as depicted in Figure S2 (left). The absorbance data were recorded at 206 nm and interpolated in a calibration curve in the concentration range of 5.3 to 87.5 µg/mL described by equation Absorbance=0.018[FER^-]-0.046 with a correlation coefficient of 0.999 (see Figure S2, right). The drug loading was estimated as 16.15 wt%, corresponding to 0.31 mol of FER^- per mol of FER@MFM-300(Sc). The result was corroborated by thermogravimetric analysis (TGA), *vide infra* (Figure S5).

The material collected was washed once with distilled water, and recovered by centrifugation. Finally, the material was resuspended in 3 mL of distilled water and lyophilised. The lyophilization process lasted 12 h and was carried out at -49 °C, with a vacuum of 0.021 Torr.

Additionally, to confirm the amount of drug loading within FERMFM-300(Sc), FER^- was quantified by using a dialysis membrane method (vide supra). The total amount of quantified FER^- was equal to 15.88 wt%, in good agreement with the initial drug loading.

Powder X-ray diffraction (PXRD)

The diffraction patterns were collected in Rigaku ULTIMA IV powder diffractometer equipped with a Lynx-eye detector using Cu Kα1,α2 radiation (λ = 1.54051, 1.54433 Å) from 2° to 30° (2θ) and a step size of 0.05° and 4 s per step in continuous mode.

N_2 adsorption isotherms

N_2 isotherms were performed on a Belsorp mini II analyzer under vacuum (10^{-3} bar). Samples of MFM-300(Sc) and FER@MFM-300(Sc) were activated at 100 °C for twelve hours and at 180 °C for two hours, respectively (under vacuum, 10^{-3} bar).

Thermogravimetric analysis (TGA)

Samples were analysed under nitrogen flow (20 mL min^{-1}) using a TGA Q5000 running from room temperature to 600 °C with a heating rate of 2 °C min^{-1} and 5 °C min^{-1}.

FTIR Spectroscopy

FTIR spectra were measured (at room temperature) using an FTIR Nicolet 6700 spectrophotometer.

NMR analysis

CP-MAS ^{13}C NMR spectra of the samples were recorded with a Bruker AVANCE III HD 300 MHz spectrometer FX-200 under the following conditions: 90° pulse, pulse width; 4 μs, pulse repetition; 5 s, pulse interval (cross polarization contact time); 7kHz spinning rate. The Chemical shift values in spectra were referenced to TMS.

Scanning electron microscopy images (SEM)

SEM were recorded using a JEOL Benchtop Scanning Electron Microscope, Neoscope JCM- 6000 using secondary electrons at 15 kV current in high vacuum.

2. *in-vitro* and *ex-vivo* studies of FER@MFM-300(Sc)

Evaluation of the *in-vitro* release of the antioxidant

The release profile of the antioxidant was obtained using a dialysis membrane method. FER@MFM-300(Sc) (30 mg) was resuspended in 1 mL of phosphate buffer saline media (PBS) (1.0 M, pH 7.4). This mixture was poured into a dialysis bag and placed into a beaker containing 100 mL of PBS (1.0 M, pH 7.4). The incubation medium was maintained under stirring (600 rpm) at 37 °C for 8 days. At pre-established times (0.5, 1, 2, 4, 6, 24, 72, and 192 h), aliquots (3 mL) were extracted, and replaced with fresh medium to maintain the "sink" conditions. The kinetics of the drug release were followed through the quantification of the drug by UV-vis spectroscopy (UV-2600, Shimadzu, put this info in general information) at a wavelength of 216 nm, previous validation of the analytical method.

After the drug-release profile experiment, we recover the solid and PXRD experiment demonstrated the retention of the crystallinity of the MOF material (Figure S3). This result corroborates that the phosphate buffer saline media (PBS) (1.0 M, pH 7.4), did not break the framework structure of MFM-300(Sc).

Cytotoxicity assays

To test whether the components of MFM-300(Sc) and the material itself might affect cell viability, human dermal fibroblasts at passage 2 were used. Cells were grown in DMEM/F12 medium (Gibco) supplemented with Fetal Bovine Serum (FBS) at 10% v/v (Gibco) and penicillin/streptomycin (Gibco) at 1% v/v. Five different concentration solutions (5, 25, 100, 250 and 500 ppm) of the components (Sc^{+3} and $BPTC^{-4}$) and MFM-300(Sc) were tested in two different cellular assays. For the first assay, solutions were prepared in double distilled water; then, 48-well culture plates were pre-treated by independently adding 100 μL of each component solutions and allowing them to dry for 2 h under sterile conditions; DMSO pre-treated culture wells were used as positive controls. Immediately after solution drying, fibroblasts were seeded (1.0 $x10^3$ cells/cm^2) in the pre-treated well culture plates and incubated with supplemented DMEM-F12 for 24 h at 37 °C and 5% of CO_2. Finally, cell viability was analysed using the LIVE/DEAD® Calcein/Etidium homidimer kit assay (Thermo) (Figure S9). For the second cellular assay, cells were seeded directly on non-treated 48-well culture plates and incubated in supplemented DMEM-F12 at 37 °C and 5% CO_2 for 24 h to allow proper cell adhesion. Then, culture medium was replaced, independently, with the different materials solutions (5, 25, 100, 250 or 500 ppm) prepared in supplemented DMEM-F12. Afterwards, the cells were further cultured for 24 h at 37 °C and 5% of CO_2. For positive controls, fresh

DMEM-12, instead of materials solutions, was added to culture wells plates. Finally, cell viability was studied using the LIVE/DEAD® Calcein/Etidium homidimer kit assay (Thermo). For both cellular tests Calcein-AM/Etidium homidimer assay was performed according to kit manufacturer guidelines. Briefly, cells were incubated with 1 µM calcein and 2 µM Ethidium homodimer for 30 minutes; then, cells were washed with PBS 1X (Gibco) and maintained in supplemented DEM-F12. Photographs were immediately acquired using an epifluorescence microscope (Zeiss) and percentage of viable cells over total number of cells was calculated from the micrographs using the Image J software.

ex-vivo permeation assay in human skin by Franz cells

Franz's cell permeation model was used to determine the permeation capacity of the FER@MFM-300(Sc), simulating a topical application of the drug. Human tissue was employed, prior approval of the letter of consent and following the guidelines of the protocol approved by the National Rehabilitation Institute (Mexico City, Mexico) #5454 and the declaration of Helsinki. The tissue was conditioned in a medium of saline solution with antibiotics and conserved in an airtight bottle at 5 °C between first 12 hours after being extracted; the thickness of the skin was 7mm. For the donor compartment, the formulations FER@MFM-300(Sc) and aqueous dispersion of FA, equivalent to 4.15×10^{-4} mol of FER^- were resuspended in 1 mL of deionized water. A control negative was established as tissue without formulation. The receptor compartment consisted of a phosphate buffer pH 7.4 that simulated a physiological medium. The experiments were conducted in a thermal bath to preserve the temperature of 37 °C, and a stirring speed of 500 rpm for 87 h. Afterwards, an aliquot of 3 mL was extracted from the receptor chamber and was analyzed by UV-Visible at 216 nm to determine the amount of the cargo that diffuses through the skin layers. The tests were carried out by triplicate. Finally, the skin samples were carefully removed from the Franz cells to conduct the tape-stripping procedure with 5 successive tape strips (Scotch® 3M®), following *in-vivo* permeation assay methodology (*vide infra*). All tapes were introduced into a flask with 15 mL of acetone, and this was mechanically stirred for 24 h. Subsequently, each skin sample was fragmented into small pieces using surgical scissors, and the drug was extracted with 15 mL of acetone (24 h). All samples were analyzed by UV-vis spectrophotometry at a wavelength of 327.5 nm.

Evaluation of the antioxidant effect of FER^- released from the MFM-300(Sc) matrix.

The antioxidant effect of ferulate (FER^-) released rom MFM-300(Sc) was evaluated using dermal skin fibroblasts donated from aesthetic surgeries (after signing the letter of informed consent), and treated according to the preestablished protocol.(Pérez-Díaz et al., 2015) The FER@MFM-300(Sc) was incubated in the culture medium for 5 days. The cells were cultured in DMEM/F12 medium (Gibco) supplemented with 10% fetal bovine serum (Gibco) and 10% penicillin/streptomycin (Gibco). To analyze the reactive oxygen species (ROS) the CellROX® kit (Thermo) was used. Briefly, 500,000 cells were analyzed, samples with MFM-300(Sc) and FA@MFM-300(Sc) were incubated during 20 minutes before incubation with H_2O_2, then incubation with hydrogen peroxide (100 mM) was also performed for 20 minutes. After incubation, staining was performed with CellRox (500 nM) and 7-AAD (10 µM, BD) for one hour following the supplier's instructions. The samples were studied in the FACS Aria III flow cytometer (BD). They were analyzed 10,000 events per experimental condition and the percentages of positive cells were obtained with the FACS Diva software (BD).

3. Molecular modelling of FER@ MFM-300(Sc)

Details of Monte Carlo and DFT Simulations

The MFM-300(Sc) crystal structure was taken from a previous experimental work (Ibarra et al., 2011) and its atomic positions were relaxed at the Density Functional Theory (DFT) level while keeping the unit cell parameters fixed. These calculations were carried out using the CP2K package (Hutter et al., 2014;

Vandevondele et al., 2005) with a plane wave energy cutoff of 500 Ry and convergence criteria on the self-consistent field interactions, maximum atomic displacement and sum atomic forces of respectively 1×10^{-6} Ry, 5×10^{-3} Bohr and 1×10^{-3} Bohr/Hartree. The atomic orbitals were treated as valence states (Goedecker and Teter, 1996; Hartwigsen et al., 1998) and their electronic exchange-correlation interactions were treated using a GGA-PBE functional (Perdew et al., 1996, 1997) combined with a double-ζ valence plus polarization (DZVP) basis set (Krack, 2005). Long-range dispersion corrections were considered using the DFT-D3 correction (Grimme et al., 2010). The atomic partial charges of all atoms of the MOF framework were calculated from this DFT optimised structure using the REPEAT scheme (Campañá et al., 2009), as implemented in the CP2K package. The atom types and their respective charges are shown in Figure S13.

The ferulate (FER^-) anion was also geometrically optimized using Na^+ as compensating cation. This optimization was carried out at the DFT level employing a GGA-PBE functional (Perdew et al., 1996, 1997) combined with a double numerical basis containing polarization functions (DNP), as implemented in the $Dmol^3$ module.(Delley, 2000). These calculations were carried out with convergence criteria on the self-consistent field interactions, maximum atomic displacement and sum atomic forces of respectively 1×10^{-5} Ha, 5×10^{-3} Å and 2×10^{-3} Ha/Å. The Na(FER) atomic charges (cf. Figure S14) were calculated using the ESP fitting approach.(Heinz and Suter, 2004)

In this study, we considered two scenarios: (*i*) low coverage adsorption of NaFER in anhydrous conditions and (*ii*) high coverage adsorption of NaFER in hydrated conditions. The first scenario had as main goal the evaluation of the main NaFER/MFM-300(Sc) interactions while the second one allowed us to access the role of the water molecules in the accommodation of the drug in the MFM-300(Sc) porosity.

Monte Carlo (MC) simulations in the microcanonical (NVT) ensemble were carried out at 310 K considering one FER^- anion and one Na^+ cation per unit cell.

Grand Canonical Monte Carlo (GCMC) calculations were first implemented at 1 bar and 310 K. to assess the amount of FER^-, Na^+ and H_2O adsorbed in MFM-300(Sc), These MC calculations were performed considering 4 unit cells (2×2×1). For each state point, 1×10^6 Monte Carlo cycles following 5×10^3 equilibration cycles (number of steps = number of cycles × number of molecules) were used as implemented in the RASPA software.(Heinz and Suter, 2004) As a second step, Monte Carlo (MC) simulations in the microcanonical (NVT) ensemble were carried out at 310 K considering the number of FER^- and Na^+ predicted in the first stage but now in the dry MFM-300(Sc) to characterize the interactions between the drug molecules and the host framework.

The interactions between the framework and the guest molecules were described considering a sum of van der Waals and electrostatic contributions modelled respectively by 12-6 Lennard-Jones (LJ) and Coulombic potentials. In the MFM-300(Sc), the LJ parameters were taken from the Dreiding (Heinz and Suter, 2004) and Universal(Buchholz et al., 2009) forcefields and respectively assigned to the atoms of the organic and inorganic nodes of the framework. The FER^- anions were considered as flexible with its bonded and LJ parameters obtained from the CGenFF forcefield (Allouche, 2012). The Na^+ LJ parameters were obtained from a previous simulation work on zeolites (Watanabe et al., 1995). Finally, water was described by the 4-site TIP4P/2005 model.(Abascal and Vega, 2005) LJ crossed parameters were calculated using the Lorentz-Berthelot rules.(Lorentz, 1881) The resulting van der Waals interactions were handled with a 12 Å cutoff while the electrostatic interactions were obtained using the Ewald summation method with a 10^{-6} precision.(Ewald, 1921; Vlugt et al., 2008) Radial distribution functions (RDFs) averaged over all MC configurations and representative

snapshots were used to evaluate the preferential interactions and adsorption sites of the guest species in the MFM-300(Sc) framework.

As a complementary, the binding energies between FER^{-} and MFM-300(Sc) in both dry and hydrated states were further calculated from DFT-optimised MC configurations. The binding energies (U_{BE}) were obtained by the following equation $U_{BE} = U_{A+B} - (U_A + U_B)$, where U_{A+B} is the energy of the adduct NaFER/MOF and NaFER/MOF/Water while U_A and U_B are the energies of each non-interacting component, *i.e.* MOF and NaFER, and MOF-H_2O and NaFER respectively.

Supplemental References

Abascal, J.L.F., and Vega, C. (2005). A general purpose model for the condensed phases of water: TIP4P/2005. J. Chem. Phys. *123*, 1–12.

Allouche, A. (2012). Software News and Updates Gabedit — A Graphical User Interface for Computational Chemistry Softwares. J. Comput. Chem. *32*, 174–182.

Buchholz, R., Kraetzer, C., and Dittmann, J. (2009). Microphone classification using fourier coefficients. Lect. Notes Comput. Sci. (Including Subser. Lect. Notes Artif. Intell. Lect. Notes Bioinformatics) *5806 LNCS*, 235–246.

Campañá, C., Mussard, B., and Woo, T.K. (2009). Electrostatic potential derived atomic charges for periodic systems using a modified error functional. J. Chem. Theory Comput. *5*, 2866–2878.

Delley, B. (2000). From molecules to solids with the DMol3 approach. J. Chem. Phys. *113*, 7756–7764.

Ewald, P.P. (1921). Die Berechnung optischer und elektrostatischer Gitterpotentiale. Ann. Phys. *369*, 253–287.

Goedecker, S., and Teter, M. (1996). Separable dual-space Gaussian pseudopotentials. Phys. Rev. B - Condens. Matter Mater. Phys. *54*, 1703–1710.

Grimme, S., Antony, J., Ehrlich, S., and Krieg, H. (2010). A consistent and accurate ab initio parametrization of density functional dispersion correction (DFT-D) for the 94 elements H-Pu. J. Chem. Phys. *132*, 154104.

Hartwigsen, C., Goedecker, S., and Hutter, J. (1998). Hartwigsen-1998. Phys. Rev. B *58*, 3641–3662.

Heinz, H., and Suter, U.W. (2004). Atomic charges for classical simulations of polar systems. J. Phys. Chem. B *108*, 18341–18352.

Hutter, J., Iannuzzi, M., Schiffmann, F., and Vandevondele, J. (2014). Cp2k: Atomistic simulations of condensed matter systems. Wiley Interdiscip. Rev. Comput. Mol. Sci. *4*, 15–25.

Ibarra, I.A., Yang, S., Lin, X., Blake, A.J., Rizkallah, P.J., Nowell, H., Allan, D.R., Champness, N.R., Hubberstey, P., and Schröder, M. (2011). Highly porous and robust scandium-based metal-organic frameworks for hydrogen storage. Chem. Commun. *47*, 8304–8306.

Ibarra, I.A., MacE, A., Yang, S., Sun, J., Lee, S., Chang, J.S., Laaksonen, A., Schröder, M., and Zou, X. (2016). Adsorption properties of MFM-400 and MFM-401 with CO2 and hydrocarbons: Selectivity derived from directed supramolecular interactions. Inorg. Chem. *55*, 7219–7228.

Krack, M. (2005). Pseudopotentials for H to Kr optimized for gradient-corrected exchange-correlation functionals. Theor. Chem. Acc. *114*, 145–152.

Lorentz, H.A. (1881). Ueber die Anwendung des Satzes vom Virial in der kinetischen Theorie der Gase. Ann. Phys. *248*, 127–136.

Perdew, J.P., Burke, K., and Ernzerhof, M. (1996). Generalized gradient approximation made simple. Phys. Rev. Lett. *77*, 3865–3868.

Perdew, J.P., Burke, K., and Ernzerhof, M. (1997). Generalized Gradient Approximation Made Simple (vol 77, pg 3865, 1996). Phys. Rev. Lett. *78*, 1396–1396.

Pérez-Díaz, M.A., Boegli, L., James, G., Velasquillo, C., Sánchez-Sánchez, R., Martínez-Martínez, R.E., Martínez-Castañón, G.A., and Martinez-Gutierrez, F. (2015). Silver nanoparticles with antimicrobial activities against Streptococcus mutans and their cytotoxic effect. Mater. Sci. Eng. C *55*, 360–366.

Vandevondele, J., Krack, M., Mohamed, F., Parrinello, M., Chassaing, T., and Hutter, J. (2005). Quickstep: Fast and accurate density functional calculations using a mixed Gaussian and plane waves approach. Comput. Phys. Commun. *167*, 103–128.

Vlugt, T.J.H., García-Pérez, E., Dubbeldam, D., Ban, S., and Calero, S. (2008). Computing the heat of adsorption using molecular simulations: The effect of strong Coulombic interactions. J. Chem. Theory Comput. *4*, 1107–1118.

Watanabe, K., Austin, N., and Stapleton, M.R. (1995). Nvestigation of the air separation properties of zeolites types a, x and y by monte carlo simulations. Mol. Simul. *15*, 197–221.